

북극 진동과 동아시아 몬순 상관성 연구

Arctic Oscillation variability and East Asia monsoon



북경사범대학교

제 출 문

극지연구소장 귀하

본 보고서를 “과거, 현재의 극지기후 관측과 재현을 통한 기후변화 메커니즘 규명 연구” 과제의 위탁연구 “북극진동과 동아시아몬순 상관성 연구” 과제의 최종 보고서로 제출합니다.



2016. 12 .

(본과제) 총괄연구책임자 : 김 성 중

위탁연구기관명 : 북경 사범대

위탁연구책임자 : 루이마오(Rui MAo)

위탁참여연구원 : 양징 (Yang Jing),
장지은(Zhang Ziyin Zhang),
공다오이 (Gong Dao-Yi)

1. To examine whether there is an interdecadal change in the relationship between AO and dust storm frequency over east Asia

Motivation and goals:

The Taklimakan Desert (TD) is located in the Tarim Basin (average elevation 1.1 km) in the northwest of China, where it is bounded by the Pamir Plateau (average elevation 5.5 km) to the west and the Kunlun Shan range (average elevation 5.5 km) and the Tian Shan range (average elevation 4.8 km) to the south and north, respectively. Dust storms mainly occur in late spring and summer over TD. Dust aerosols being transported from TD can have an important role in the global dust background level owing to the high elevation and long-lasting nature of the transport. On a global scale, the dust particles from the TD could influence global radiation budget by stimulating cirrus cloud formation and marine ecosystems by supplying nutrients to the open ocean.

Arctic Oscillation (AO)/North Atlantic Oscillation (NAO) is a dominant mode in the mid-high latitudes of the Northern Hemisphere. Many authors found that AO/NAO in spring or former winter has a tight relationship with the dust storm frequency (DSF) over the TD. However, there may occur some uncertainty in the AO-DSF relationship over the TD. On one hand, Gao et al [2010] found an negative correlation between AO and dust activities in April over TD during 1980-1992, by merit of Total Ozone Mapping Spectrometer (TOMS) Aerosol Index. Rather, on an interannual timescale, Mao et al [2010] showed an in-phase relationship between AO and DSF over the TD during spring in the period 1982-2006, by using observational data and numerical simulations. On the other hand, we hypothesized that the AO/NAO-DSF relationship may have an interdecadal change during past decades and then shows different correlations during different periods. Recently, some studies found that AO/NAO-East Asian climate relationship experienced a significant interdecadal change in the late 1970s and early 1990s [e.g., Kwon et al., 2005; Gong et al., 2011; Chen et al., 2014; and Gao et al., 2014]. In the present study, we will present evidences to show that the connection between spring AO and DSF in April to July experienced a pronounced interdecadal change at the beginning of the 1980s on an interannual timescale.

Work done and findings

1) Temporal changes in AO-DSF relation

The DSF over the TD increases from January, reaching its peak during April to July, and then decreases. As compared with annual average of DSF of 24.8 days during 1961-2007, DSF from April to

July accounts for 52% of the annual average (12.8 days). Thus, the DSF during April to July (AMJJ) was analyzed in this paper. We averaged the AMJJ DSF and its 21-yr sliding relationship with spring AO index was analyzed (Fig. 1a). The sliding correlation for spring AO index and AMJJ DSF is unstable during the period 1961-2007; there are a significant negative correlation before early 1980s and a weakening one afterward and a positive one in the early 1990s. This result confirms that the relationship between spring AO and AMJJ DSF experienced an interdecadal change, i.e., significant negative correlation before early 1980s and insignificant negative or positive correlation afterward. We calculated the correlation between AMJJ DSF and spring AO index before and after early 1980s, respectively. The correlation coefficient between spring AO index and AMJJ DSF is -0.44 and 0.30 during 1961-1983 and 1984-2007, respectively; the former one is significant at the 95% confidence level (Fig. 1b).

2) *Distinct spring AO-associated features in two epochs*

Based on the identified interdecadal change in the early 1980s in the AO-DSF relationship, we selected two subperiods, 1961-1983 (P1) and 1984-2007 (P2), to explore the AO-associated features over Asia. In P1 epoch, when spring AO is in a negative phase, there are positive height anomalies during April to July over northwestern China and western Mongolia in the lower troposphere (1000 hPa), with a center locating through the boundary between northwestern China and western Mongolia. The positive height anomalies over northwestern China and western Mongolia suggest increased cold air activities there. Moreover, the circulation anomalies in the mid troposphere provides a favorable condition for the formation of cold front at the surface during P1 epoch. The most prominent feature in the mid troposphere is negative height anomalies over western Siberia and northeastern China and positive height anomalies over Tibetan Plateau and the Mid East in the mid troposphere (Figure 2a). These height anomalies suggest that an negative AO phase is associated with intensified high-pressure (low-pressure) systems over Tibetan Plateau and the Mid East (western Siberia and northeastern China).

During P2 epoch, the AO-associated atmospheric circulation anomalies in the mid troposphere were analyzed. There is a cyclonic height anomaly over western Siberia but with the southwestward relocation and increased intensity as compared with that for P1 epoch (Figure 2b). And there occur a positive height anomaly covering central Siberia and northwestern China. Besides the negative height anomaly over western Siberia, there also occur a negative height anomaly over Mid East. This anomalous circulation distribution is favorable for the dust weather occurrence over the TD. The negative height anomaly over western Siberia indicates frequent low-pressure system activities there, and the negative height anomaly over Mid East means the low-pressure system over western Siberia frequently moving southward, which brings warm air from low latitude to the TD and then causes an establishment of heat low-pressure systems over TD. Subsequently, the low-pressure system over western Siberia creates short wave troughs that move

eastward and bring cold air mass from polar to the northern boundary of TD. When the cold air mass accompanied by short wave troughs cross over the TianShan Mountains, a strong temperature gradient is formed between the inflow cold air and a warm air in the Tarim basin. Then the cold airflow has the characteristics of a gravity current, inducing a strong surface wind. As a result, dust storms appear in the Tarim Basin [Chen et al., 1999; Aoki et al].



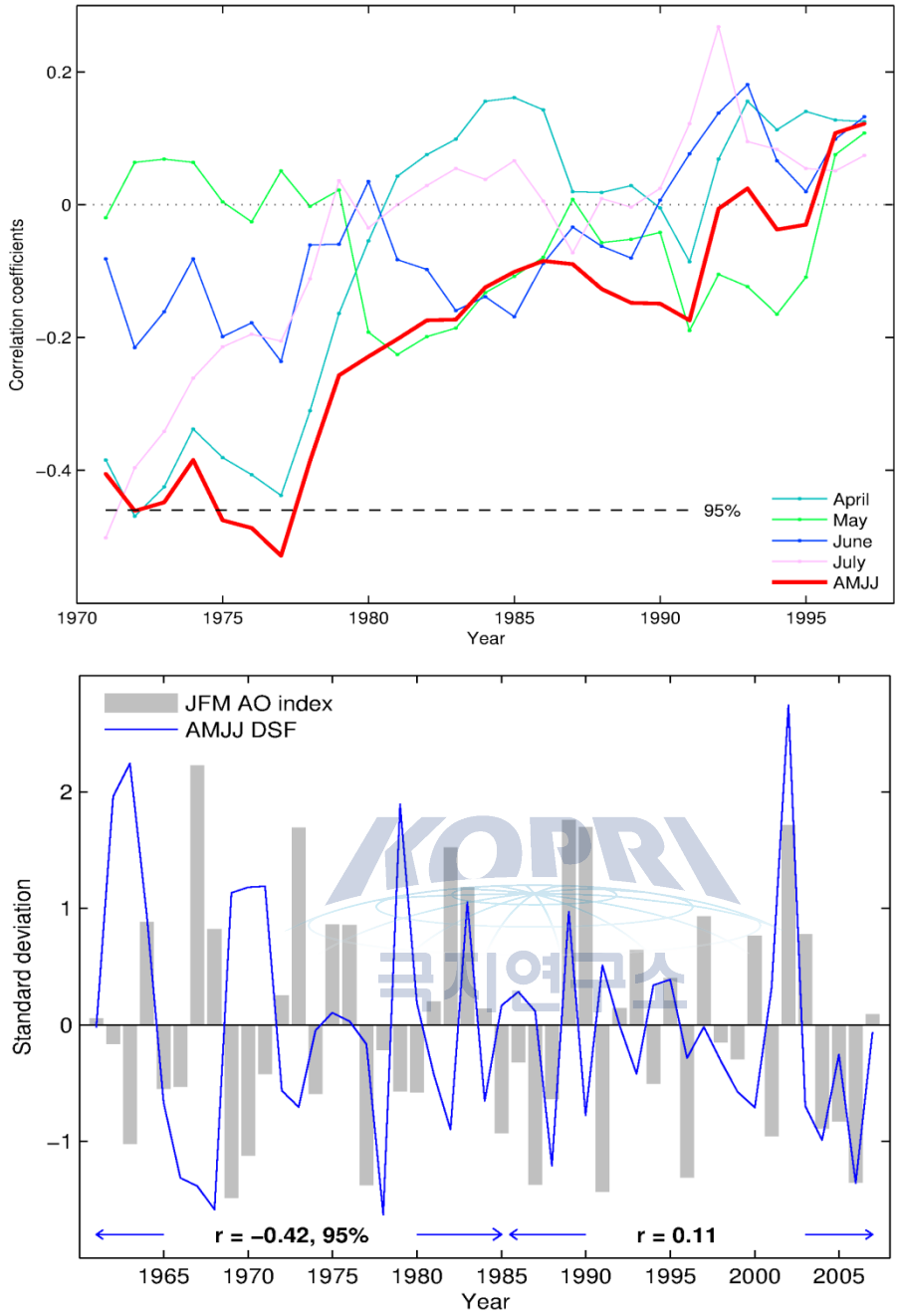


Fig. 1 The running 21-yr correlation between AO and DSF over TD (a). Time series of AO and DSF during April to July over TD (b).

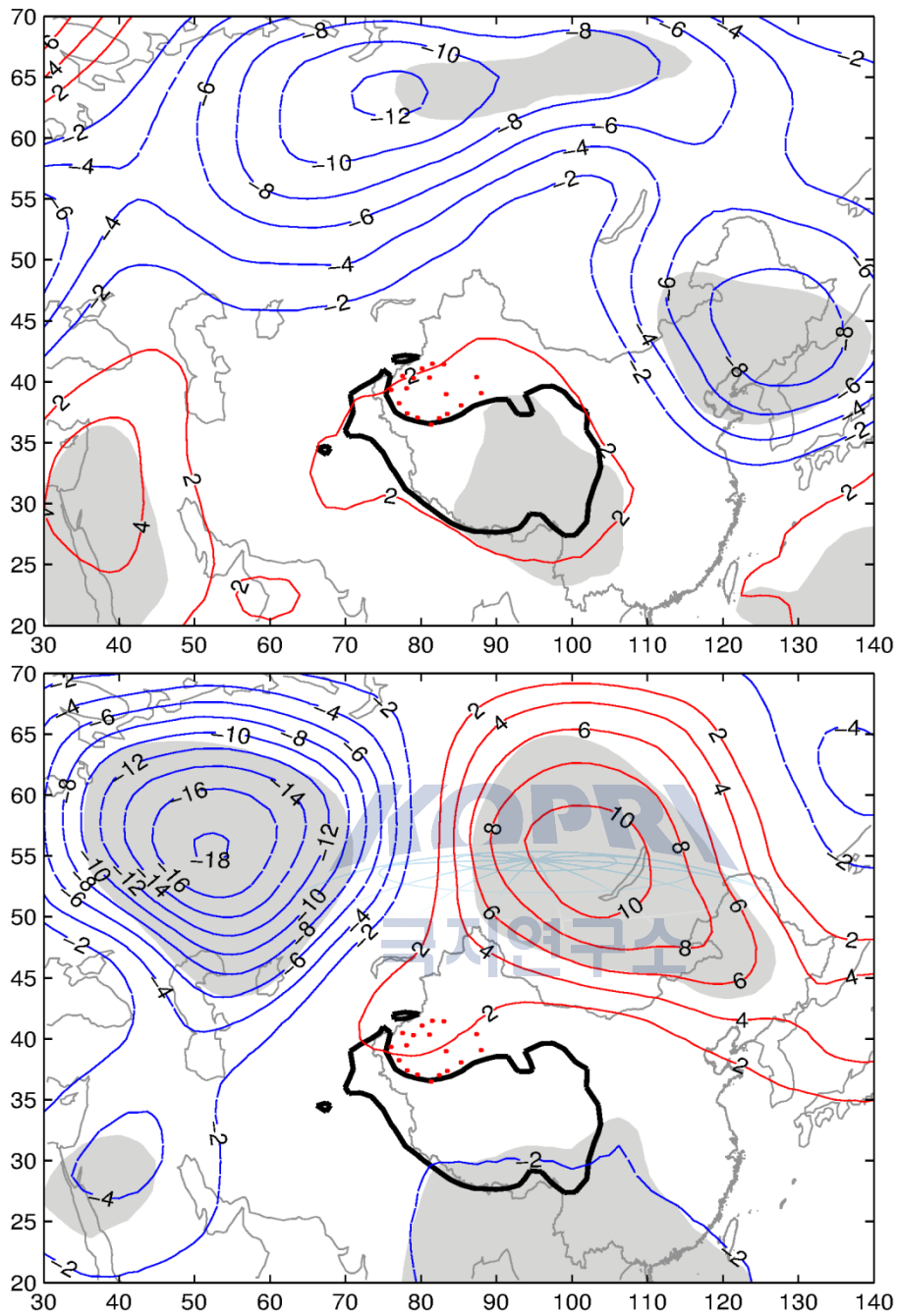


Fig. 2 Regression of 500-hPa height during April to July against AO index in April and May for P1 (1961-1983) and P2 (1984-2007). Significant at the 95% confidence level are shaded. Positive (negative) values are solid (dashed) lines.

2. *Objective: Boreal winter Arctic Oscillation as an indicator of summer SST anomaly over western tropical Indian Ocean*

Motivation and goals:

The sea surface temperature (SST), particularly the tropical SST, is one of the key factors contributing to multi-seasonal to inter-annual climate predictability. Indian Ocean SST variability plays important roles in monsoonal climates. Previous studies found that the El Niño/Southern Oscillation (ENSO) and Indian Ocean Dipole (IOD) are two primary modes generating inter-annual variability of oceanic and atmospheric climates over the Indian Ocean and beyond with a certain persistence. On the other hand, oceanic dynamics as the leading processes in sustaining and propagating the temperature (in particular the subsurface temperature) variations are well recognized. For example, the equatorial oceanic Rossby wave is important in forming TIO variability at time scales ranging from intraseasonal to inter-annual. Local or remotely connected wind stress anomalies dynamically cause regional Ekman pumping and further generate the forced Rossby wave.

In addition to tropical forcings, the mid- high latitude circulation such as Arctic Oscillation (AO)/North Atlantic Oscillation (NAO) is also found to influence TIO climates on intraseasonal to inter-annual times scales. Recent studies showed that during positive AO/NAO winters the enhanced Arabian High brings anomalous northern winds over the northern Indian Ocean, the enhanced crossing-equator air-flow results in simultaneously anomalous western winds, more-than-normal precipitation, and a deeper thermocline in the central TIO. In this study we report that during the following summer of positive winter AO, the SST over the western TIO experiences significant warming due to the arrival of oceanic Rossby wave which is generated in central Indian Ocean by anomalous AO-related wind stresses in winter.

Work done and findings

3) *Significant correlations between AO and SST*

Firstly, we investigated the possible SST anomalies in association with JFM AO in a straightforward manner by simply computing the ERSST regression upon the JFM AO index. To focus on the possible time-lags we considered SSTs for every two-month segments from March through October. Instead of random noises, we found that there are clear structures in the anomalous SST fields. During March-April the majority of SST anomalies are of the negative, which are likely due to the JFM AO-related air-sea flux (Gong et al., 2014). In May-June the negative SSTs are replaced by the positive anomalies in tropical

Indian Ocean west of 60E. The significant warming becomes much stronger in July-August, being >0.2C in a large region west of about 55E (Figure 1). The signals in the western TIO sharply weaken in September-October and disappear afterward.

Note that the regression analysis is performed based on the residuals after high-pass filtering and removal of ENSO/IOD. The AO-SST linkage, if physically robust, should emerge in the raw observations. Furthermore, the correlation/regression analysis ignores the possible non-linearity of the links. For clarification we additionally examined the SST composites based on JFM AO index. The difference of positive means minus the negative means is computed, and the corresponding significance is estimated using two-sample t-test. As shown in Figure 2, we found that slightly positive anomalies appear in western TIO west of 55E in May-June, but the SST warming is not statistically significant. Interestingly, in the following July-August significant positive SST anomalies appear in the western TIO, the >0.2C anomalies cover a large region of about 7S-7N west of 65E with a maximum of >0.4C west of 55E. The location and spatial extent of the significant SSTs in summer are almost identical to the regression analysis. Generally, composites display features highly similar to the regression analysis, likely manifesting the winter AO-summer SST linkage again.

To reveal the details of the SST anomalies through the seasons we further investigated the monthly SST variations. Based on regression analysis we selected a region of 10S-10N and 40°-60E, where the largest SST anomalies are located, to make a regional mean SST time series. Then the cross-correlations of JFM AO index with the SST time series are computed for each month. The correlation increases substantially from spring to summer (Figure 3). The three largest correlations appear in July (0.70), August (0.60) and June (0.49), all are significant at the 0.01 level. After October the correlations become insignificant. As shown in Figure 4, the regional mean summer SST strongly co-varies in-phase with JFM AO index, their correlation coefficient is 0.71. Note the feature of SST correlations increasing from spring to summer. We defined this multi-month SST tendency as SST difference (Δ SST) of June-July-August minus April-May. The SST tendency is correlated with JFM AO at $r=0.75$ (Figure 4).

4) Prediction models using AO, ENSO and IOD

The high correlation between AO and SST implies the JFM AO index is of practical implication because it could serve as a potential predictor of summer western TIO SST anomalies. We developed two simple statistical prediction models for the regional mean SST and its tendency. The regional mean SST and Δ SST are the target predictand, which to be predicted by three predictors including the means of the preceding winter and autumn IOD index, the preceding winter Niño3.4 SST, and the JFM AO index. By fitting to all data samples during the period 1979-2015, we obtain the corresponding prediction equations as follows:

$$SST = -0.36IOD + 0.25Ni\tilde{n}o3.4 + 0.16AO; \quad \text{and}$$

$$\Delta SST = -0.33IOD + 0.04Ni\tilde{n}o3.4 + 0.18AO - 0.01$$

The SST 'prediction' model yields a high correlation against the observation ($r=0.81$), and the ΔSST model has a similar correlation ($r=0.79$), suggesting these two models respectively explain $r^2=65\%$ and $r^2=62\%$ of the observation variance. We might conclude that among all three terms in our prediction model the JFM AO is a major contributing factor for the inter-annual changes of summer SST and ΔSST (see also Figure 3).

5) Possible mechanisms

The analysis of AO-related surface heat fluxes show that the net heat flux cannot explain the western TIO warming since the significant negative net fluxes indicates ocean losing heat to atmosphere. Whereas the ocean dynamics play dominant roles. Due to the wind stress curl in positive AO winters, the downwelling Ekman pumping forces a deeper thermocline and above-normal SSH in central TIO between 60 and 75E where the climatological depth of the thermocline is shallowest in Indian Ocean tropics. The forced downwelling Rossby wave propagates westward at a speed of about 0.14ms^{-1} . Its arrival at the western TIO results in significant warming of uppermost water. Forced by the observed AO wind stress anomalies over Indian Ocean, the BCM model well reproduce the Rossby wave and the consequent JJA SST warming over the western TIO, supporting the importance of the oceanic dynamics in connecting winter AO and anomalous summer SSTs.



Table 1. Anomalous JJA surface heat fluxes over western tropical Indian Ocean in association with JFM AO index during 1984-2009. Unit: Wm^{-2}

Regions	Qnet	SW	LW	SH	LH
10°N-10°S, 40-60°E	-5.54 [#]	+1.54	-1.86	-0.45*	-4.70 [#]
5°N-5°S, 40-55°E	-7.92 [#]	+0.19	-0.93	-0.63*	-6.73 [#]

* significant at the 0.1 level, [#] at the 0.05 level

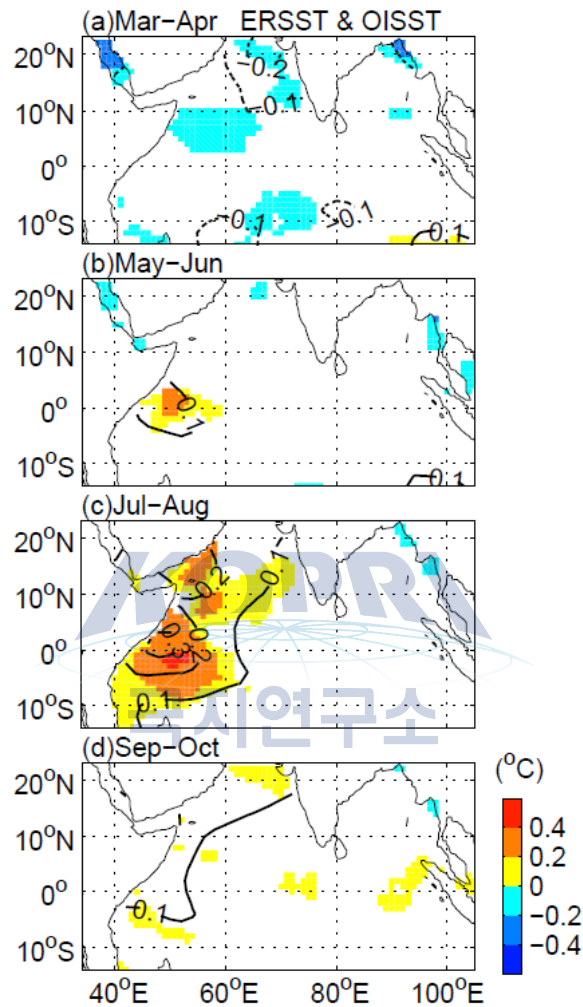


Figure 1. SST changes from March through October in association with JFM AO index. The OISST anomalies are shown as colors (only values significant at the 0.05 level are plotted) and the ERSST anomalies are overlaid as contour lines with unit of $^{\circ}\text{C}$. OISST period is 1982-2015, and ERSST data period is 1979-2015.

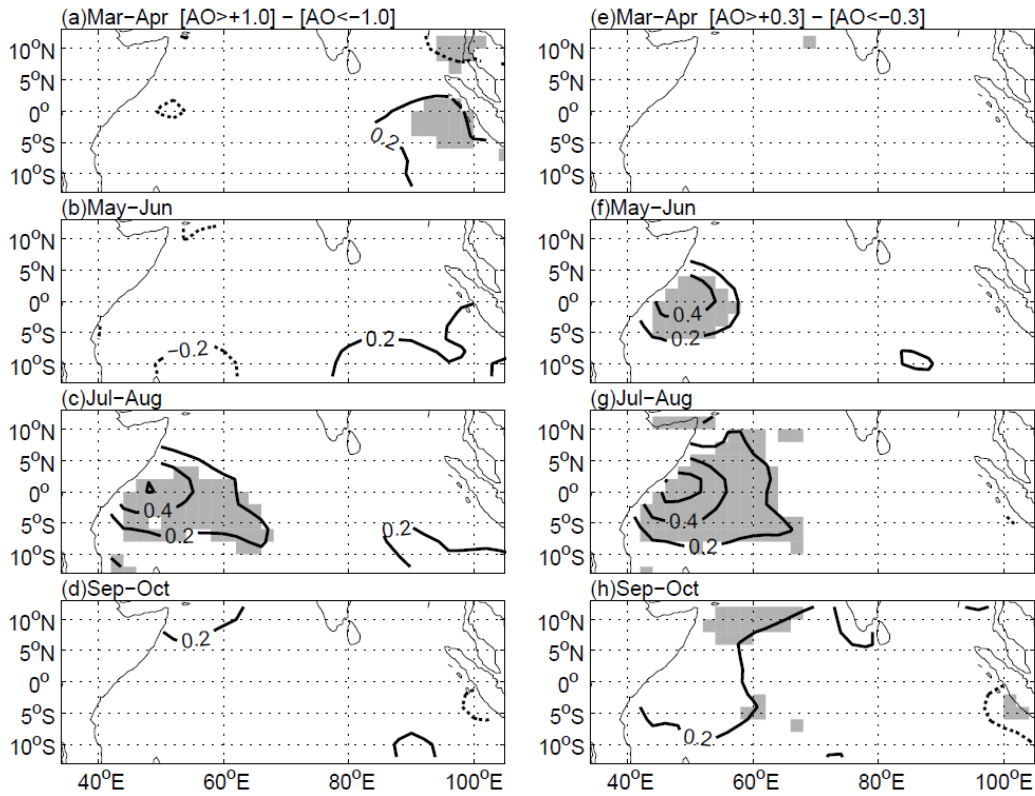


Figure 2. SST differences of the positive AO years minus the negatives. The positive AO cases are defined as $AO > +1.0$ (or $+0.3$), and the negatives as $AO < -1.0$ (or -0.3). Positive SST differences are shown as solid contour lines and the negatives as the dashed lines. The significance levels are estimated from two-sample t -test and values above the 0.05 level are indicated by gray shadings. Results are based on the original, unfiltered ERSST during period 1979-2015.

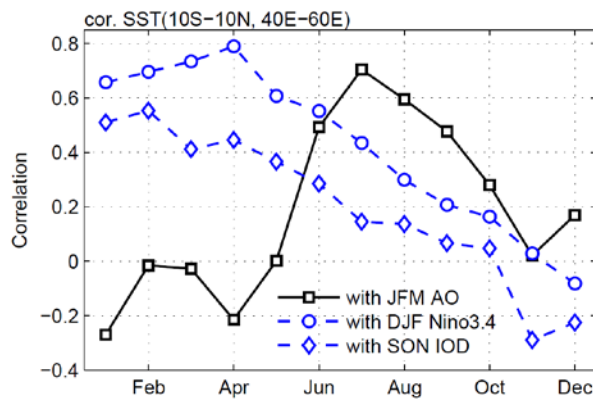


Figure 3. Correlations between JFM AO index and monthly ERSST anomalies from January through December over western tropical Indian Ocean during 1979-2015. The correlations with Niño3.4 SST and IOD are plotted together for comparison.

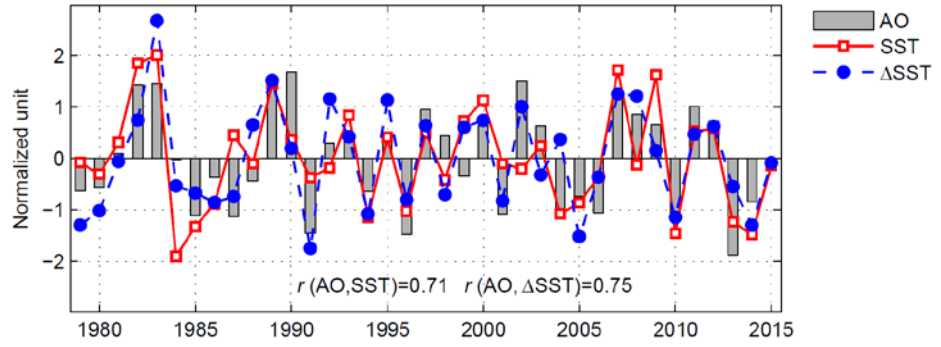


Figure 4. Timeseries of regional mean JJA SSTs and SST tendency over western tropical Indian Ocean (10°S-10°N, 40-60°E). The JFM AO is plotted together for comparison. Multi-month SST tendency (Δ SST) is defined as the SST anomaly difference of June-July-August minus April-May. All are normalized to facilitate comparison.

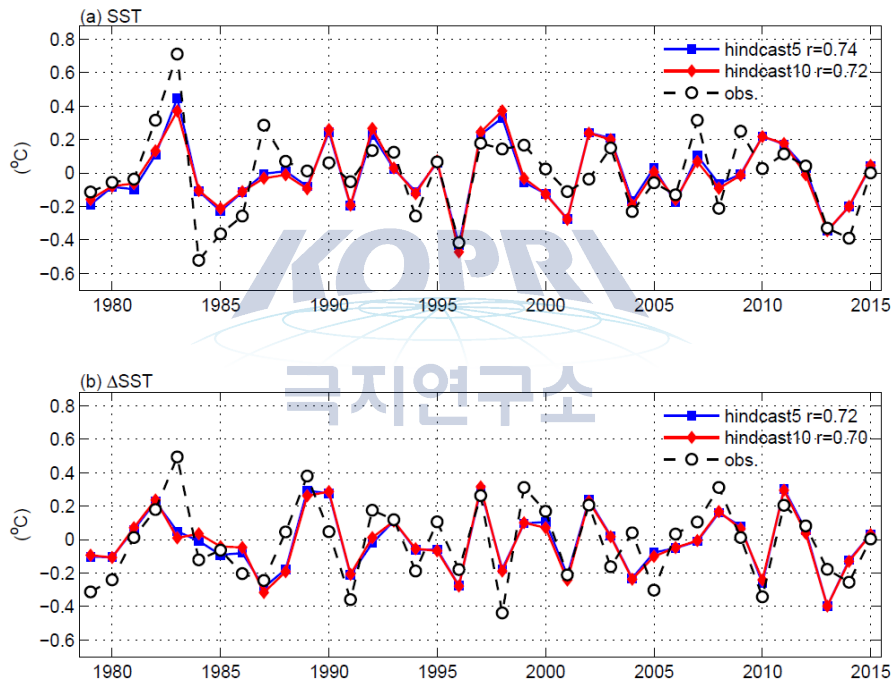


Figure 5. Interannual SST and Δ SST anomalies in JJA as predicted using the preceding JJA AO index, the preceding winter Niño 3.4 SST and the preceding autumn-winter IOD index. Predictions shown here are made based on a leave-5-cross-validation and a leave-10-out cross-validation, labeled as 'hindcast5' and 'hindcast10' respectively.

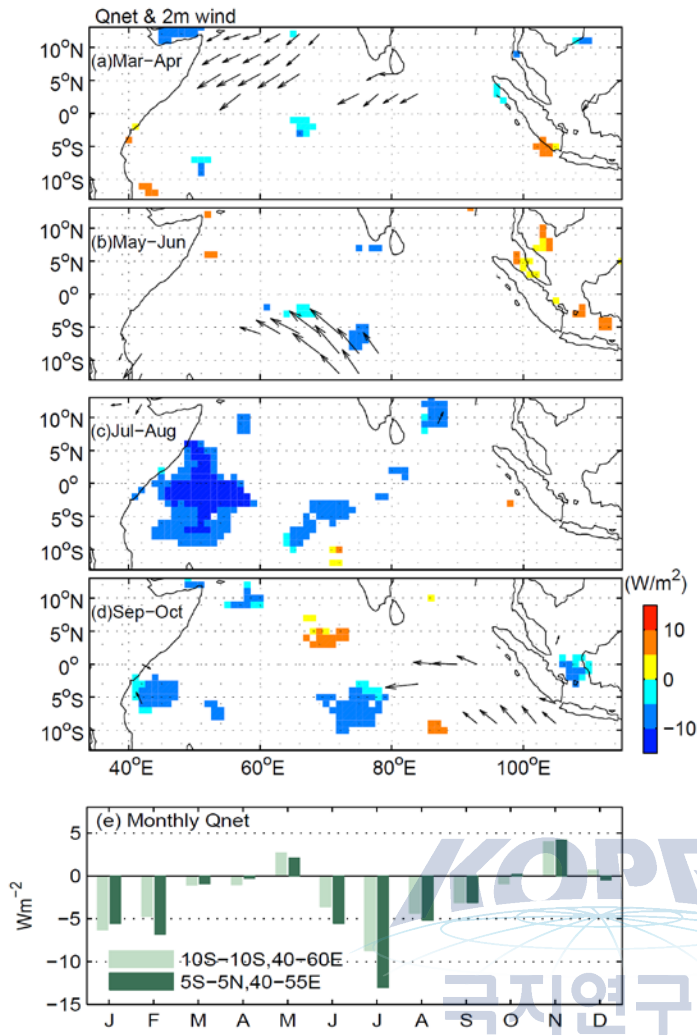


Figure 6. Net surface heat fluxes (Qnet, colors in a,b,c, d) from March through October in association with JFM AO index. Vectors in a,b,c, dare anomalous 2m wind velocities from ERA-Interim, and the maximum vector is $0.7ms^{-1}$. Only significant at the 0.05 level Qnet and winds are plotted. The regional mean monthly Qnet anomalies averaged over western tropical Indian Ocean are shown in (e).

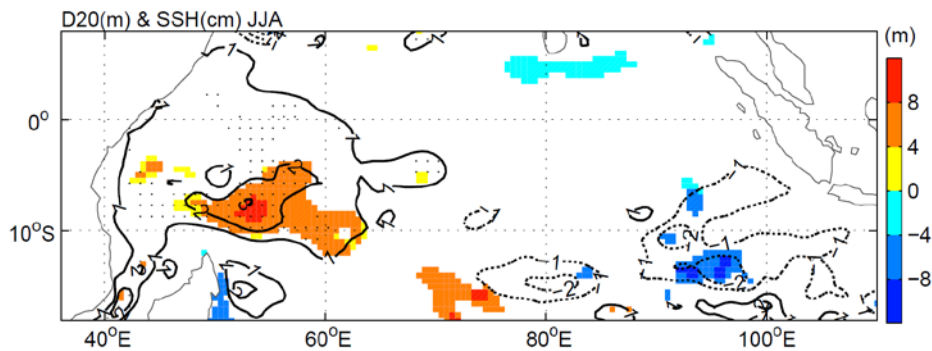


Figure 7. Anomalies of June-July-August 20°C isotherm depth (D20, colors, in meters) and sea surface height (SSH, contour, in centimeters) in association with JFM AO index. Zero contours are omitted for clarity. Only significant D20 at the 0.05 level are shown. Significant SSHs are indicated by stipples.

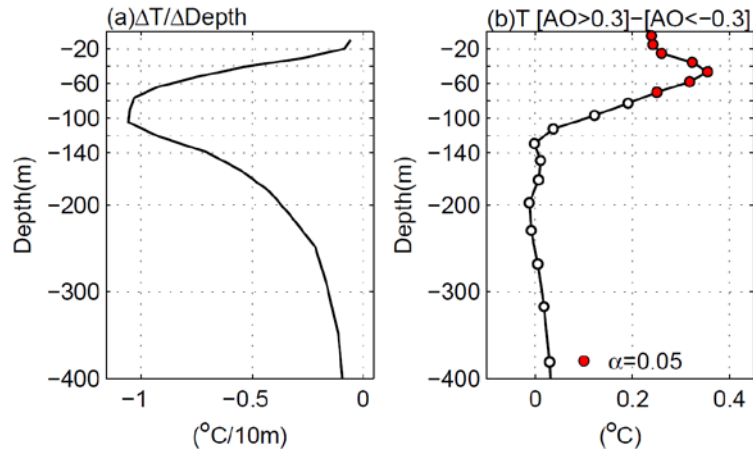


Figure 8. (a) Long-term mean vertical temperature gradients, (b) the temperature difference of positive AO years ($\text{AO} > +0.3$) minus the negatives ($\text{AO} < -0.3$). Analysis season is June-July-August, shown are regional means averaging over $40\text{-}60^{\circ}\text{E}$ and $10^{\circ}\text{S}\text{-}10^{\circ}\text{N}$. Filled cycles indicate the significance level of 0.05.

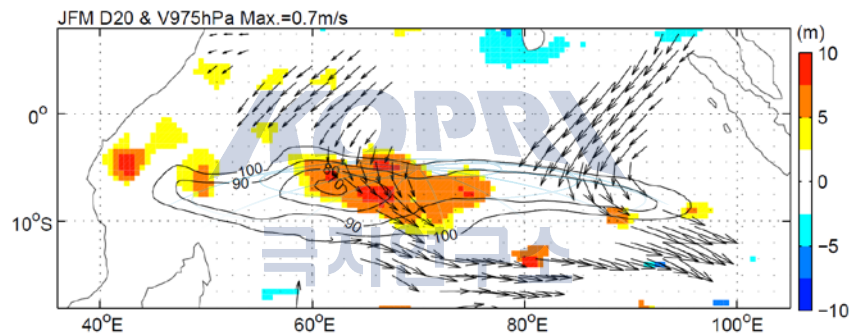


Figure 9. Anomalies of the 20°C isotherm depth (contour shadings, in meters) and ERA-Interim 975hPa horizontal winds (vectors, in m s^{-1}) corresponding to one unit of AO index during JFM. The long-term mean depth of 20°C isotherm smaller than 100m are overlaid as contour lines. Only anomalous winds and isotherm significant at the 0.05 level are plotted.

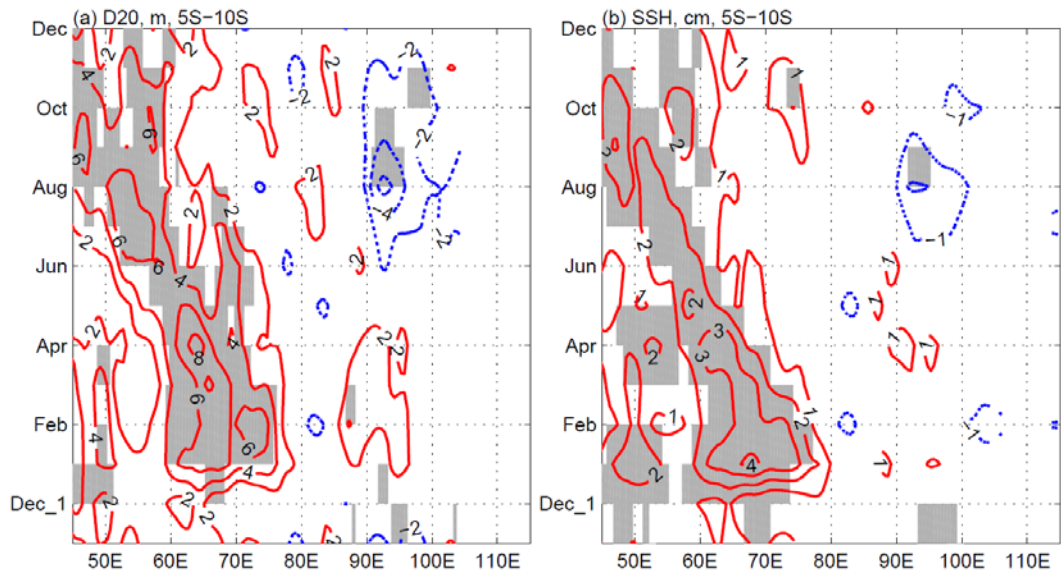


Figure 10. (a) Anomalous 20°C isotherm depths and (b) sea surface heights between 5-10°S in association with one unit of JFM AO index. Significant at the 0.05 level values are indicated by shadings.

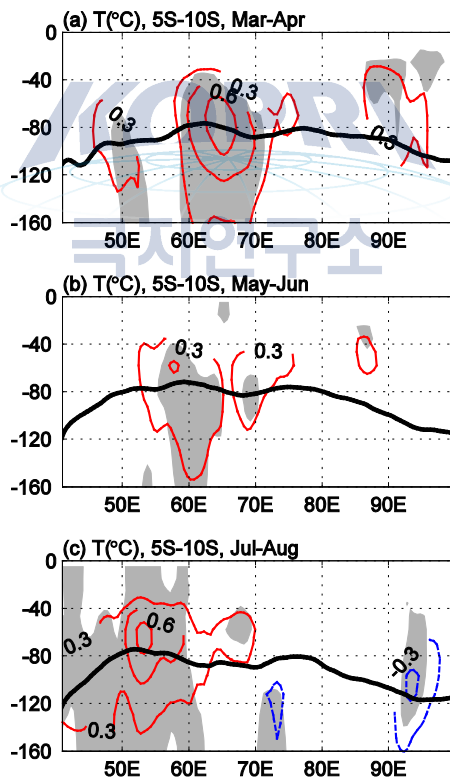


Figure 11. Anomalies of sea water temperature between 5-10°S in association with one unit of JFM AO index for each two-month segments from March through August. Significant at the 0.05 level values are shaded. Solid lines indicate the long-term mean depth of 20°C isotherm.

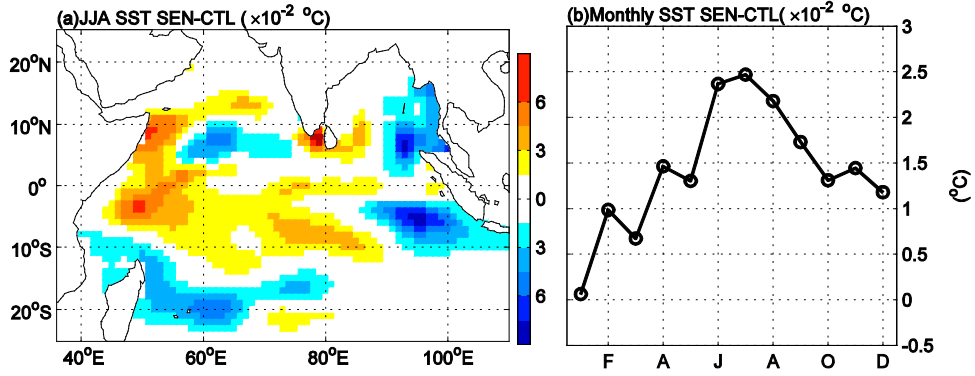


Figure 12. (a) SST anomalies as the difference of sensitivity runs minus the control runs during JJA, and (b) the regional mean differences averaged over the western Indian Ocean (40-60°E and 10°S-10°N) from January through December.

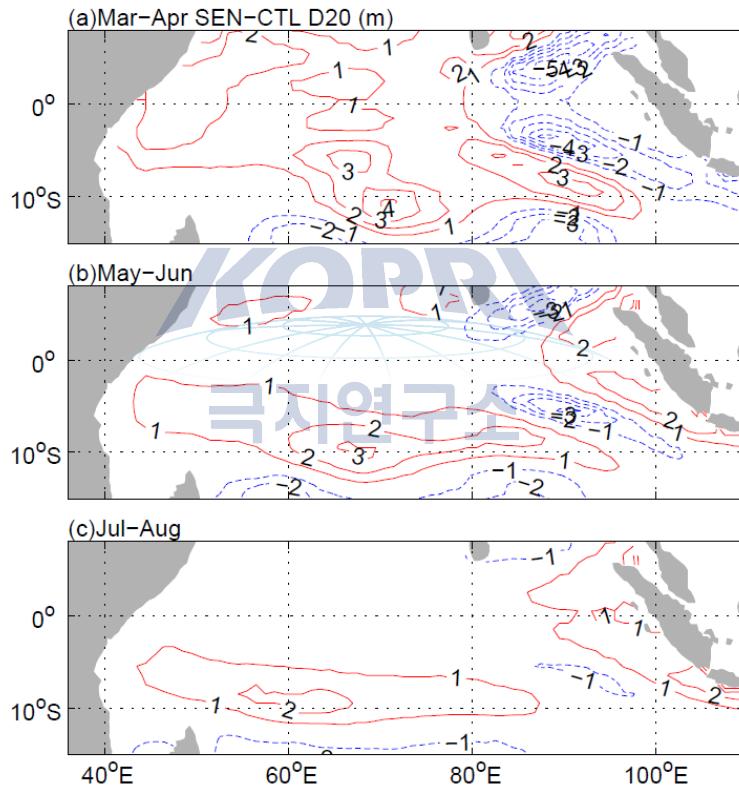


Figure 13. Simulated 20°C isotherm depth difference of sensitivity runs minus the control runs by BCM2.0. Shown as the two-month segments from March through August. Zero contours are omitted for clarity.

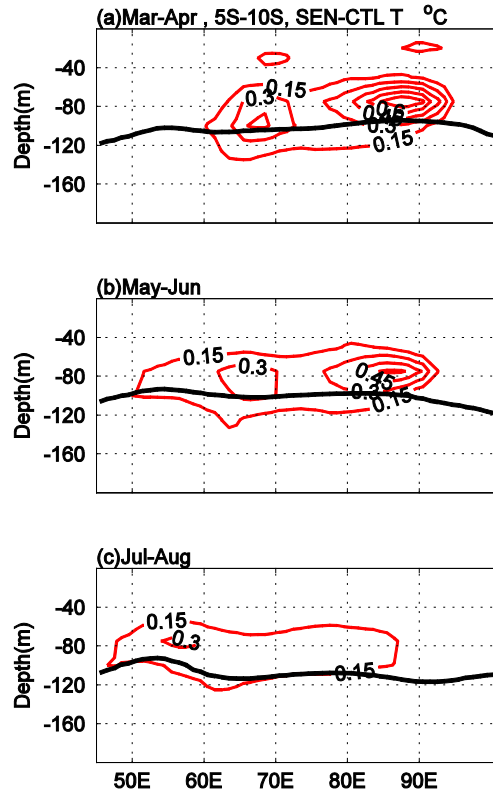
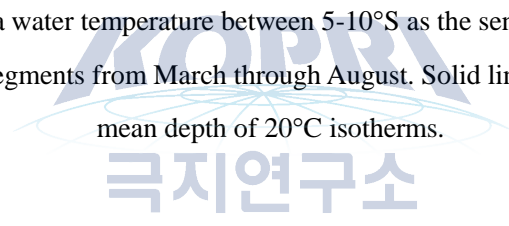


Figure 14. Difference of sea water temperature between 5-10°S as the sensitivity runs minus the control runs for each two-month segments from March through August. Solid lines indicate the model climate mean depth of 20°C isotherms.



3. Objective: Interannual modulation of East African early short rains by winter Arctic Oscillation

Motivation and goals:

Following the seasonal migration of the intertropical convergence zone, the equatorial East Africa exhibits two peaks of precipitation every year. One takes place around March-May (i.e., the long rains), and the other occurs around October to December (i.e., the short rains). Although the short rains bring less precipitation than the long rains (Figure 1), they have a higher interannual variability with recurrent droughts and floods such as that of 1997, 2005, 2010 [e.g., Hastenrath, 2007, 2010; Liebmann et al., 2012; Philippon et al., 2015]. Improving our understanding of the short rains variability is of important implication for the livelihood of millions.

Evidence shows that the winter Arctic Oscillation (AO) can exert influence on tropical climates over western North Pacific and Indian Ocean on the interannual timescale. In association with boreal winter AO, an atmospheric Rossby wave train emanates from the North Atlantic, propagates southeastward, and reaches the Asian subtropical jet stream. That produces an anomalous anticyclonic atmospheric circulation over North Indian Ocean which results in a cross-equatorial air-flow for positive AO cases. The anomalous anticyclonic atmospheric circulation there drives anomalous westerlies to the west and easterlies to the east, the resultant convergence of the moisture transport leads to above-normal precipitation over East Africa. Therefore, in the present study we present evidence that the East African early short rains are modulated by boreal AO through the persistent anomaly of the upper ocean heat content and the atmospheric moisture and convection over the western Indian Ocean.

Work done and findings

- 1) A significant in-phase covariation relationship was found between the JFM AO index and the October precipitation over the equatorial East Africa*

After high-pass filtering the precipitation timeseries and linearly removing the ENSO and IOD variance, the anomalies of the monthly precipitation rates corresponding to the JFM AO index were computed. A significant in-phase covariation relationship was found between the JFM AO index and the October precipitation over the equatorial East Africa. All data sets show no any significant anomaly over East Africa and the neighboring Indian Ocean in November. In September, the significant anomalies below

4mm/day appear in a few scattered grids over western Indian Ocean, especially in GPCP and CMAP datasets. In contrast, the precipitation anomalies in October display an evident pattern with a quite spatial coherence among all data sets. The salient feature is the significant positive autumn precipitation anomalies over the equatorial East Africa under positive winter AO phase. The location and extent of the anomalies are generally similar among the 4 datasets, approximately covering a key region between 5°S-5°N and east of 35°E, where the maxima are about 0.4-0.8mm day⁻¹ in association one unit of the JFM AO index. We further examined the temporal features of the precipitation. As shown in Figure 3, the October EARI (as averaged over 5°N-5°S and 35°-35°E) shows well in-phase year-to-year variations with the JFM AO index. The precipitation maxima of 1982, 1997, 2009, and 2011 co-occur with strong positive AO, while in anomalously dry years of 1996, 2010, and 2013 the JFM AO indices are quite low. Indeed, the Pearson correlation between October EARI and the JFM AO is +0.51. After the IOD and Niño3.4 SST signals have been removed, their correlation still remains +0.46. Both are statistically significant at the 0.05 level.

2) *The local/regional moisture transport and the active convection result in above-normal precipitation over the equatorial East Africa.*

The changes in both the atmospheric circulation and troposphere humidity are analyzed (i.e., these variables are high-pass filtered first, and afterwards, the IOD and ENSO variance are linearly removed, and finally are regressed upon the JFM AO index). Dominant feature is the significant increase in the water vapor in the western Indian Ocean between about 0°-10°S. The maxima of >0.8kg m⁻² extend from about 65°E to the coast. In the majority of the equatorial East Africa east of 35°E the values are between 0.4-0.8kg m⁻². Even in the inland area west of 30°E between 0°-5°N, there are positive anomalies <0.4 kg m⁻². At 850hPa there is no significant wind anomaly, consistent with the results of composite analysis. It is clear the anomalous water vapor is unlikely brought by large-scale anomalous atmospheric circulation horizontal transport or convergence. The AO-related vertical air motion at 500hPa indicate significant ascending along about 5°S west of 55°E. The location of strong ascending and the anomalous water vapor are almost identical in the western Indian Ocean, suggesting the in-situ evaporation and convection plays a major role.

This is further supported by the anomalous vertical profiles of the vertical motion and humidity. Anomalous specific humidity is located below 650hPa with a maximum of 0.2-0.4g kg⁻¹ between 850-700hPa centering at 5°S. The significant upward motion is located between 0°-7°S and extends from 850hPa to 250hPa with a maximum of 0.37m s⁻¹. The longitude-height section along 4.5°S reveals that the positive humidity anomalies spread from lower troposphere upward to 200hPa in association with strong ascending between 40°-50°E. Smaller positive humidity anomalies can also be found to the east in about

60°-75°E. Note that the background circulation in October is the overwhelming southeasterly, which transports the anomalous moisture horizontally from the western Indian Ocean westward into the East African continent [e.g., Chan et al., 2008; Mutai and Ward, 2000]. Therefore, the local/regional moisture transport and the active convection result in above-normal precipitation over the equatorial East Africa. In addition, some synoptic systems that origin in the western Indian Ocean may penetrate into the coastal continent in the presence of strong southeastern winds, and produce precipitation along their development over the continent [Mutai and Ward, 2000].

3) *Possible mechanisms*

A mechanism linking the winter AO and early short rains is suggested. The JFM AO-related atmospheric circulation is characterized by a simultaneous enhanced cross-equatorial air-flow in central Indian Ocean. This C-type wind stress anomaly forces a downwelling oceanic Rossby wave between 60°-75°E and 5°-10°S, where the thermocline significantly deepens by >4m and the sea surface height is about 2cm above normal. The subsurface temperature changes significantly, accompanying the westward propagation of the Rossby wave along the thermocline. In February, the center of the subsurface warming is between about 65°-75°E. Then it moves to 60°-65°E and 55°-60°E in April and June, respectively. The Rossby wave arrives in western Indian Ocean in late summer, resulting in significant warming of >0.6°C west of 55°E in depth of 60-100m. This warming remains significant through October. Afterwards the temperature anomalies between 40°-60°E weaken rapidly and disappear in December. Corresponding to the subsurface warming the upper ocean heat content significantly increases in October by about $2-3 \times 10^8 \text{ J m}^{-2}$ in a region west of 60°E between 5°-10°S. The upper ocean heat content enhances atmospheric moisture and convection over the western Indian Ocean leads to the more-than-normal precipitation over the downstream equatorial East Africa in the presence of background southeastern winds.

The role of the oceanic dynamics in linking winter AO and anomalous subsurface warming over the western Indian Ocean was tested by the numerical experiments using an oceanic general circulation model. The experiments were performed with the forcing of AO-related wind stress anomalies over Indian Ocean in winter. The oceanic Rossby wave generated in central Indian Ocean during boreal winter, its westward propagation, the associated subsurface warming, and the anomalous upper ocean heat content in October over the western Indian Ocean all are well reproduced.

Table 1. Correlations among October East African precipitation (EARI), the upper ocean heat content in the top 150m (HC150), and the January-February-March AO index. In parentheses are correlations after removing ENSO and IOD variance. The HC150 is averaged over 40°-60°E and 5°-10°S.

	AO(JFM)	HC150 (Oct.)	EARI (Oct.)
AO (JFM)	\	+0.49*	+0.51*
HC150 (Oct.)	(+0.50)*	\	+0.45*
EARI (Oct.)	(+0.46)*	(+0.53)*	\

* significant at the 0.05 level

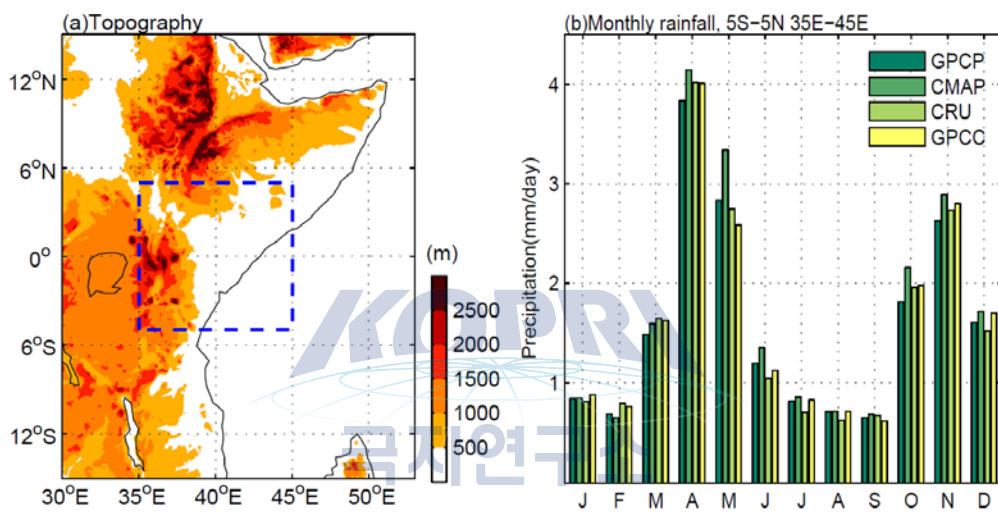


Figure 1. (a) Topography of East Africa, (b) long-term means of the monthly precipitation over the region of 5°S-5°N and 35°-45°E with respect to 1981-2010. Target region is shown as the box in (a).

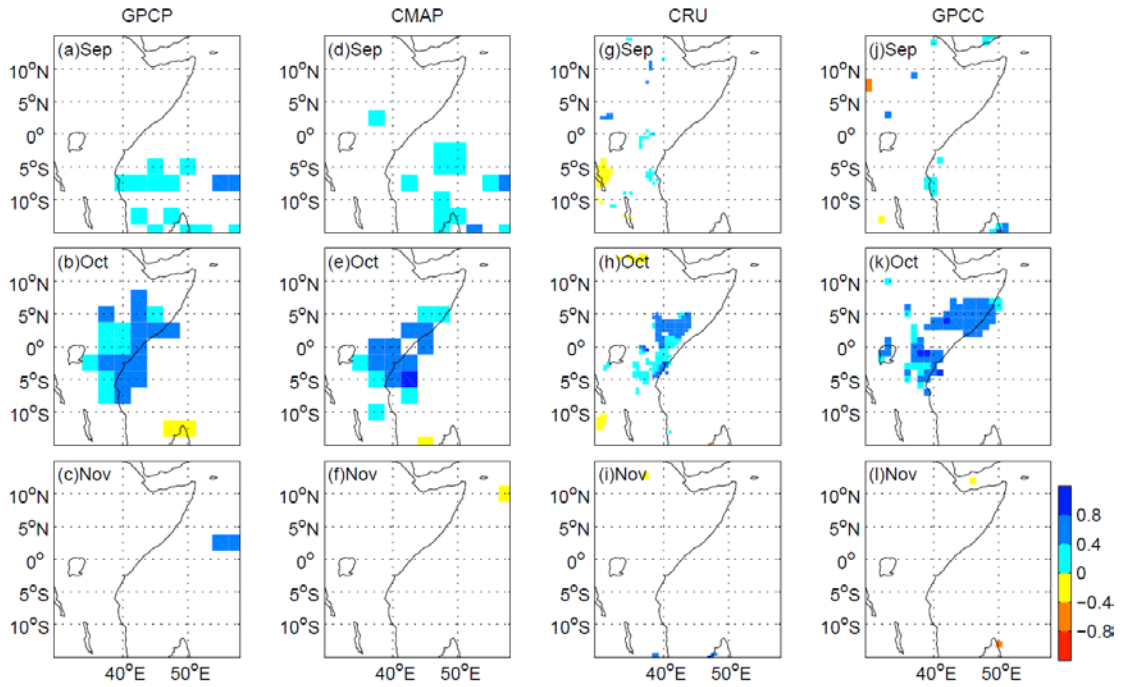


Figure 2. Interannual precipitation anomalies from September to November in association with the JFM AO index. All of GPCP, CMAP, CRU, and GPCC are analyzed using the same period of 1979-2014. Only values significant above the 0.05 level are shown. Unit: mmday^{-1} .

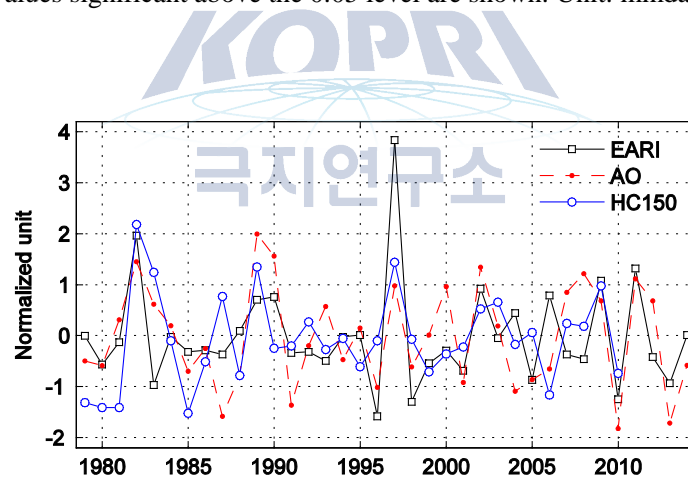


Figure 3. Time series of the JFM AO index, October East African rainfall index (EARI), and the ocean heat content in the uppermost 150m (HC150) averaged over 40° - 60° E and 5° - 10° S. All timeseries are normalized with respect to the whole data period to facilitate comparison.

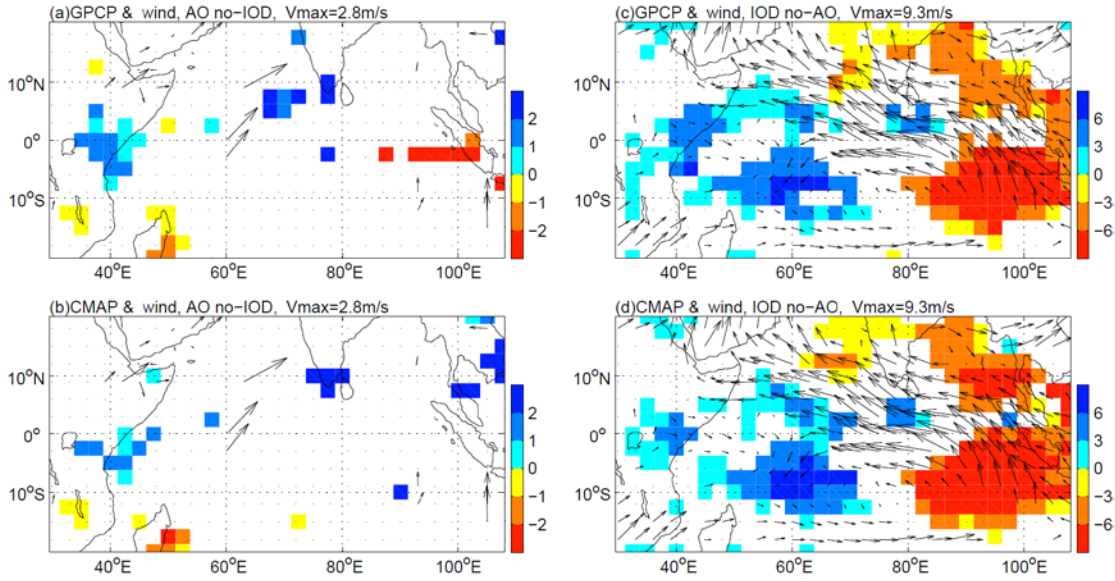


Figure 4. Composites of precipitation in October based on the JFM AO indices (a,b) and the autumn IOD indices (c,d). Precipitation anomalies are shown in colors with unit of mmday^{-1} . Horizontal wind vectors at 850hPa are superimposed. Only values significant at the 0.1 level are plotted.

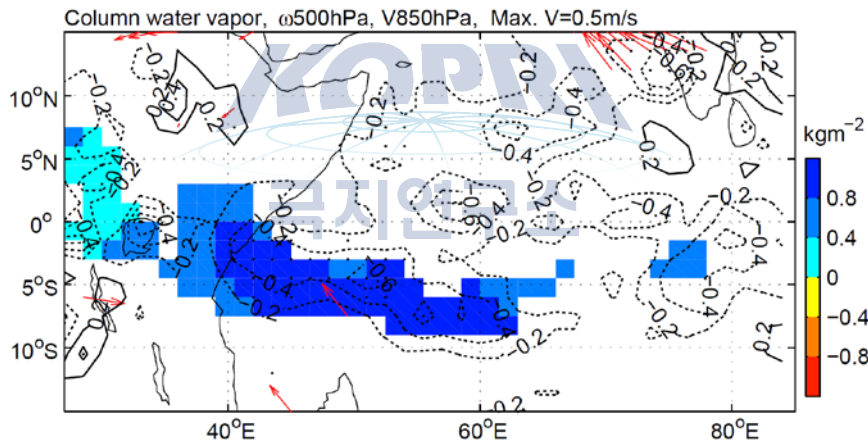


Figure 5. Anomalies of the total column water vapor (colors, kgm^{-2}), 850hPa horizontal winds (vectors, ms^{-1}), and 500hPa vertical velocity (contours, 10^{-2} Pa/s) in association with the JFM AO index. Only significant (at the 0.05 level) water vapor and 850hPa winds are shown. Significant vertical motion is indicated by stipples.

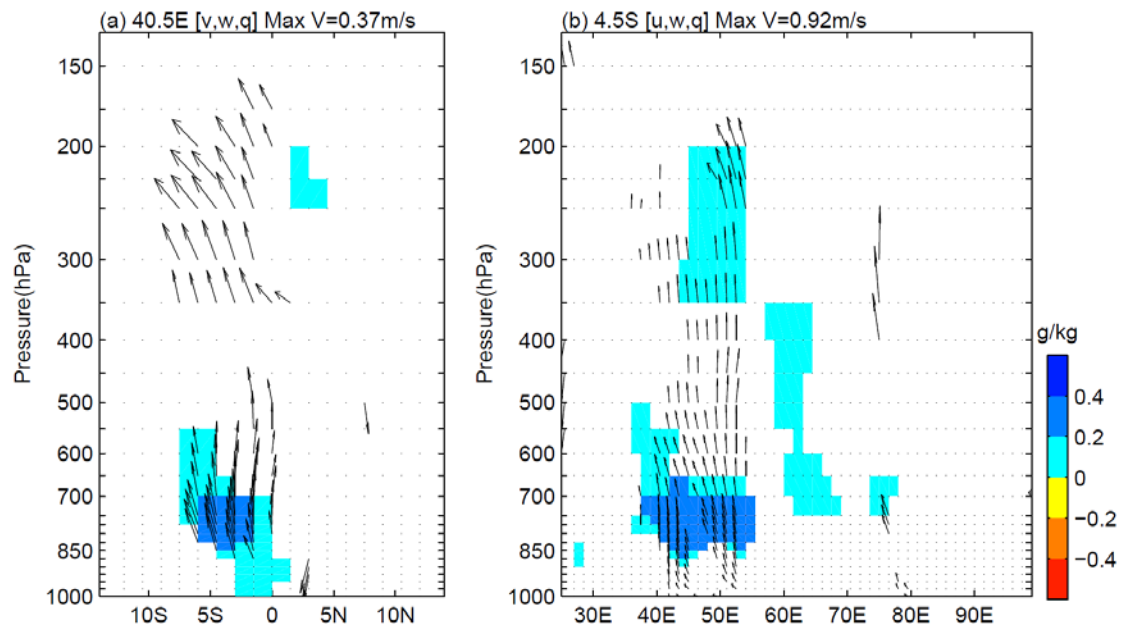


Figure 6. Anomalies of wind velocity and specific humidity in the latitude-pressure section along 40.5°E (a) and in the longitude-pressure section along 4.5°S (b). Only values significant at the 0.05 level are shown.

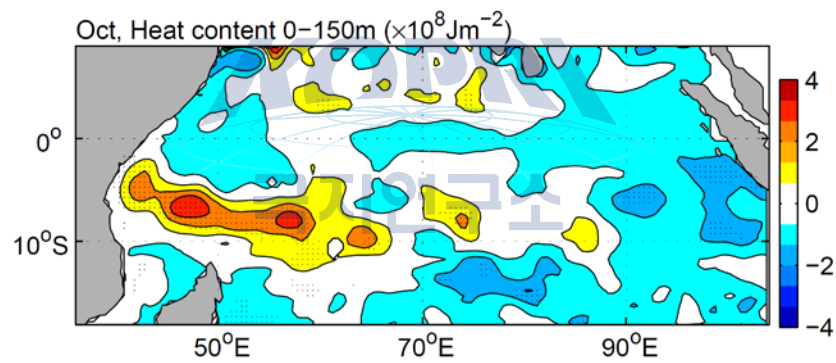


Figure 7. Heat content anomalies in association with the JFM AO index. Stipples denote values significant at the 0.05 level.

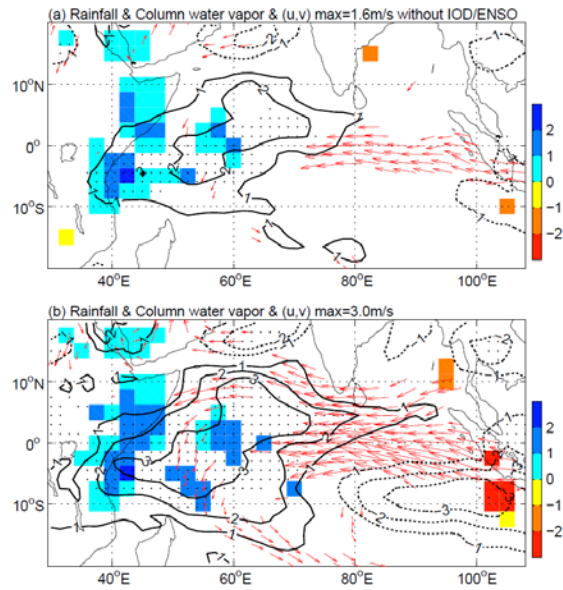


Figure 8. Anomalous GPCP rainfall (colors, mm day^{-1}), total column water vapor (contours, kg m^{-2}), and 850hPa horizontal winds (vectors, ms^{-1}) in association with the regional mean upper ocean heat content over $40^{\circ}\text{-}60^{\circ}\text{E}$ and $5^{\circ}\text{-}10^{\circ}\text{S}$. Only significant (at the 0.05 level) GPCP and winds are plotted. Significant total column water vapor is denoted by stipple. In (a) the IOD and ENSO variance have been removed and in (b) not removed.



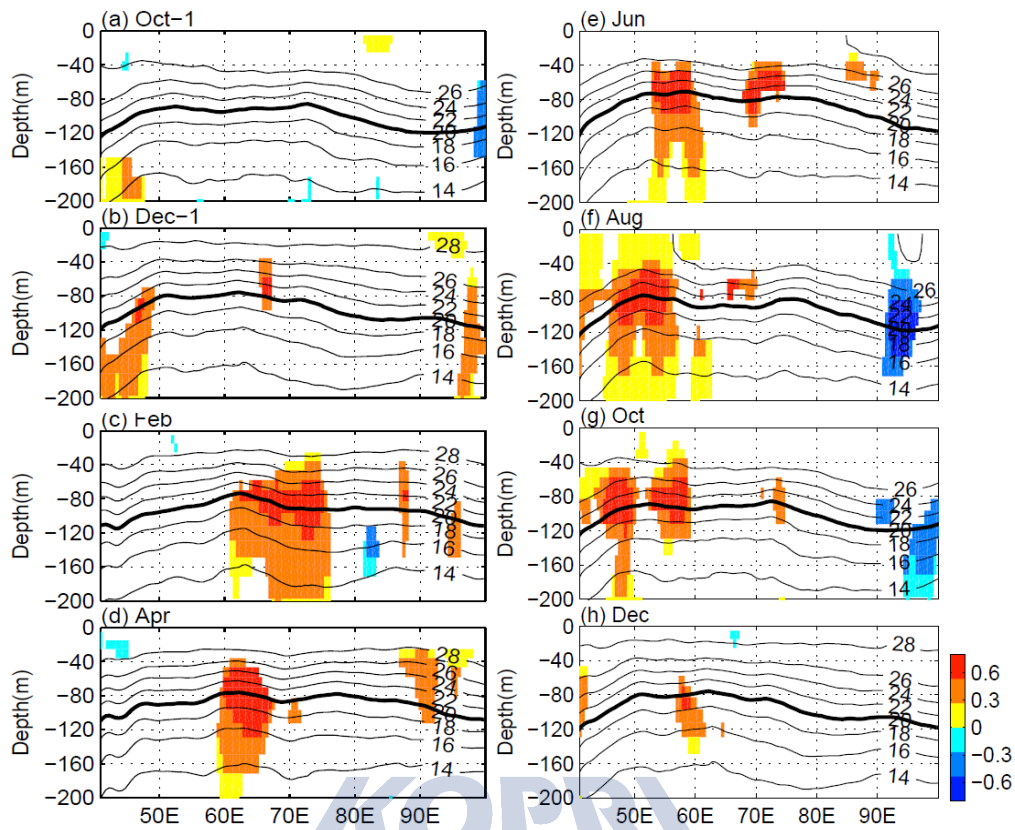


Figure 9. Temperature anomalies in association with the JFM AO index from preceding October to the concurrent December plotted for each other month. Contour lines are long-term mean temperature, and the 20°C isotherm depth is shown in bold line. Color shadings denote significant values at the 0.05 level.

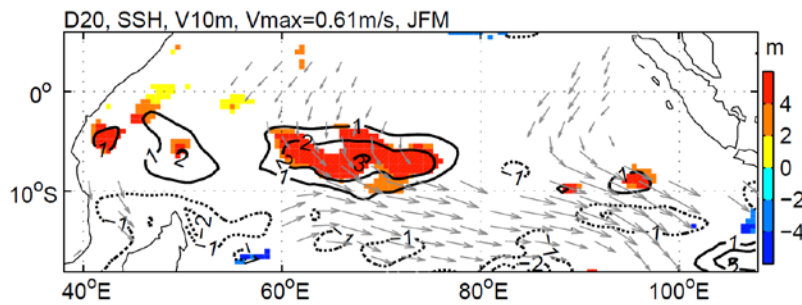


Figure 10. Anomalous ERA-Interim 10m winds (vectors with units of ms^{-1}), 20°C isotherm depth (D20, colors with units of m), and sea surface height (SSH, contours with units of cm) in association with the JFM AO index. Plotted D20 and winds both are significant at the 0.05 level.

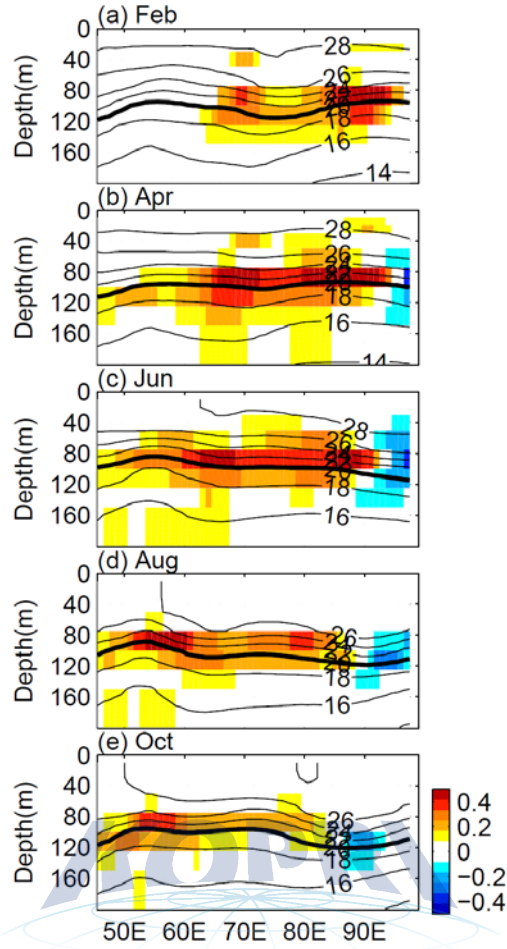


Figure 11. Simulated temperature changes averaged from 5°-10°S in response to the JFM AO wind stress forcing. The long-term means of the temperature are superimposed as contours, and the 20°C isotherms are shown in thick lines. Unit: °C

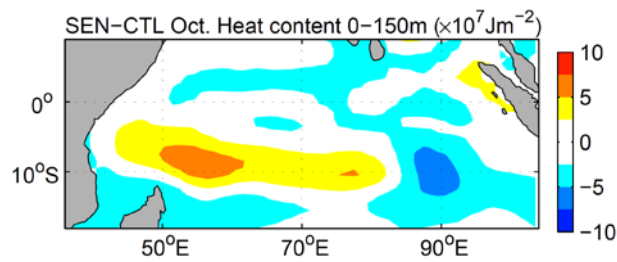


Figure 12. Simulated changes of the ocean heat content in the upper most 150m in October. Shown as the difference of the sensitivity minus the control runs based on 100 ensembles.

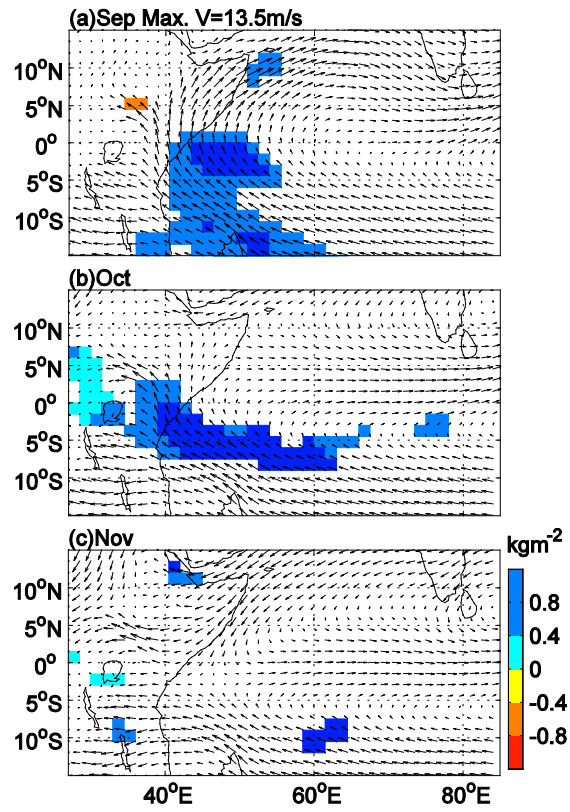
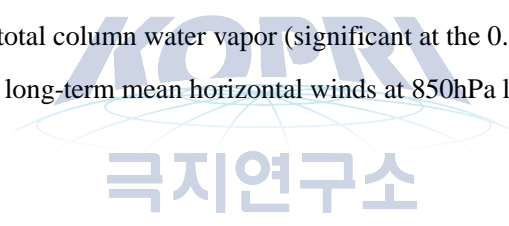


Figure 13. Anomalies of the total column water vapor (significant at the 0.05 level) in association with the JFM AO index. The long-term mean horizontal winds at 850hPa level are superimposed.



4. *Objective: To investigate the possible reason for the model skills of simulating the spring AO-associated cyclonic anomaly over Western North Pacific*

Motivation and goals:

The seasonal prediction of the East Asian summer monsoon (EASM) has been a challenging scientific issue due to the distinctive and complex geography of this region (Hsu *et al.*, 2014). The Arctic Oscillation (AO) has pronounced effects on East Asian climate (e.g., Gong *et al.*, 2002; Yang *et al.*, 2012; Chen *et al.*, 2013; Yun *et al.*, 2014). In terms of mid to high latitudinal preceding signal for the EASM prediction, several previous studies have reported that the spring AO could influence the EASM on an interannual timescale by modifying the underlying surface thermal conditions over the Eurasian continent (e.g., Shen and Masahide, 2007) and the north Atlantic SSTs (e.g., Wu *et al.*, 2009). Recently, several studies have shown that the western Pacific local air-sea anomalies imposed by the spring AO play a predominant role on maintaining the spring AO signals through the following summer and consequentially affecting the EASM (Gong *et al.*, 2011; Gao *et al.*, 2013; Chen *et al.*, 2014). According to Gong *et al.* (2011), in the positive phase of the AO, an anomalous cyclone occurs over subtropical North Pacific (between 120°E–160°W) in the lower-troposphere. The anomalous westerly winds of this cyclone decrease the total wind speed over tropical central northern Pacific and warm the tropical ocean surface via the reduced surface evaporation and wind stirring. The warming SST in turn excites ascending atmospheric Rossby waves that reinforce the cyclonic anomaly in their journey to the west from spring to summer. Thus, the anomalous cyclonic circulation over western North Pacific (WNP) maintains to the following summer due to the above-mentioned positive air–sea feedback and leads to the weakened WNP subtropical high (WNPSH) as well as an eastward retreat of the WNPSH, which further weakens the EASM.

The climate model is an indispensable tool to make seasonal predictions. However, whether the current climate models can reproduce the spring AO-EASM connection remains unknown, which is one of the key steps to recognize climate models and improve the EASM prediction. Therefore, this study aims to address two questions: (1) Are the CMIP5 models able to reproduce the spring AO-WNP connection? (2) What is responsible for the model skills in simulating the spring AO-WNP connection?

Work done and findings

4) Spring AO – WNP connection in CMIP5 models

The spring AO-WNP connection is evaluated based on 16 CMIP5 models. The results indicate that half of the models reproduce this connection, while the other half of the models do not reproduce this connection. Accordingly, the models are categorized into two groups. The first group of models retains the AO signals over the WNP from spring to summer because they reproduce the formation of the spring AO-associated WPCA as well as its persistence through the following summer. The second group of models fails to simulate the spring WPCA so that lose the spring AO signals over the WNP. As a result, it is crucial for a model to reproduce the spring AO-associated WPCA to establish the linkage between the spring AO and the EASM.

5) Spring AO-associated NPAD is crucial to the Spring AO – WNP connection in CMIP5 models

Further analyses show that the establishment of the spring WPCA is closely related to the presence of the NPAD. If the spring AO-associated NPAD is reproduced, the spring WPCA also forms in simulations; vice versa. The simulated NPAD may be related to the simulated subtropical westerly jet over the East Asia- WNP and transient eddy activities near the westerly jet exit region. Additionally, the air-sea interaction over the WNP plays an important role in maintaining the WPCA from spring to summer according to previous studies. Therefore, another study is currently being conducted to compare AMIP (Atmospheric Model Intercomparison Project) and CMIP parallel models to verify the role of the WNP air-sea coupling in the connection between the spring AO and the EASM.

Table 1 Details of the 16 CMIP5 models used in this study

Model	Institute, Country	Resolution (horizontal, vertical) AGCM/OGCM
BNU-ESM	College of Global Change and Earth System Science, Beijing Normal University, China	128×64L26/ 360×200L50
MPI-ESM-P	Max Planck Institute for Meteorology (MPI-M), Germany	192×96L47/ 256×220L40
CanESM2	Canadian Centre for Climate Modelling and Analysis, Canada	128×64L35/ 256×192L40
CESM1-BGC	National Center for Atmospheric Research, America	192×288L26/ 320×384L60
CESM1-CAM5		192×288L26/ 320×384L60
CESM1-FASTCHEM		192×288L26/ 320×384L60
CMCC-CM	Centro Euro-Mediterraneo per I Cambiamenti Climatici, Italy	480×240L31/ 182×149L31
CNRM-CM5	Centre National de Recherches Meteorologiques/Centre Europeen de Recherche et Formation Avancees en CalculScientifique, France	255×128L31/ 362×292L42
FGOALS-g2	LASG, Institute of Atmospheric Physics, Chinese Academy of Sciences and CESS, Tsinghua University, China	360×180L26/ 360×196L30
INMCM4	Institute for Numerical Mathematics, Russia	180×120L21/ 360×340L40
IPSL-CM5A-LR	Institut Pierre-Simon Laplace, France	96×96L39/ 182×149L31
HadCM3	Met Office Hadley Centre, United Kingdom	96×73L19/ 288×44L20
IPSL-CM5B-LR	Institut Pierre-Simon Laplace, France	96×96L39/ 182×149L31
MIROC-ESM-CHEM	Science and Technology, Atmosphere and Ocean Research Institute (The University of Tokyo), and National Institute for Environmental Studies, Japan	128×64L80/ 256×192L44
MIROC5	The University of Tokyo, National Institute for Environmental Studies, and Japan Agency for Marine-Earth Science and Technology, Japan	256×128L40/ 256×224L50
MPI-ESM-LR	Max Planck Institute for Meteorology (MPI-M), Germany	192×96L47/ 256×220L40

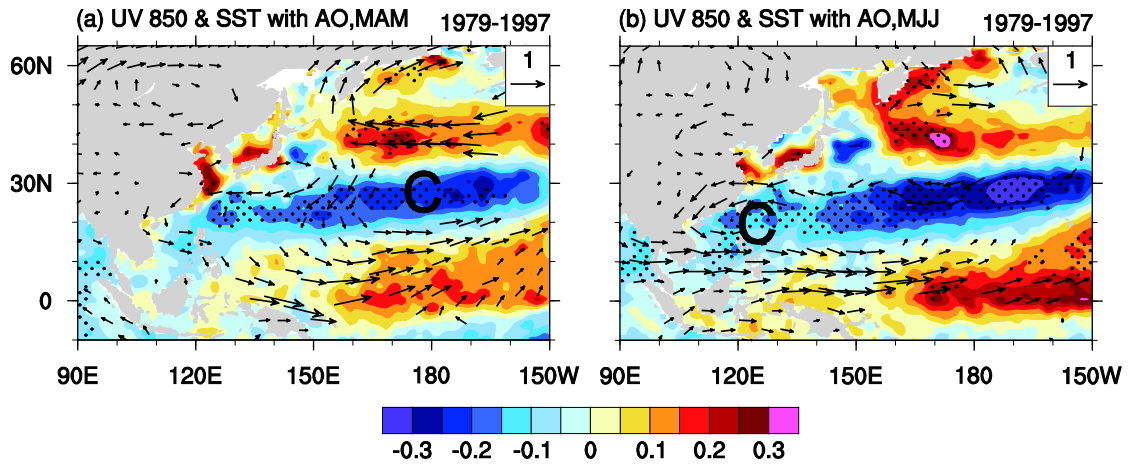


Fig. 1 Regressed 850-hPa wind (vectors: m/s) and SST (shadings: degree) anomalies against the spring AO index based on the ERA-interim reanalysis, respectively, in (a) MAM and (b) MJJ. The areas exceeding the 90% confidence level are dotted, and only the wind vectors that are statistically significant above 90% based on a t-test are plotted. 'C' denotes the center of the cyclonic anomaly.



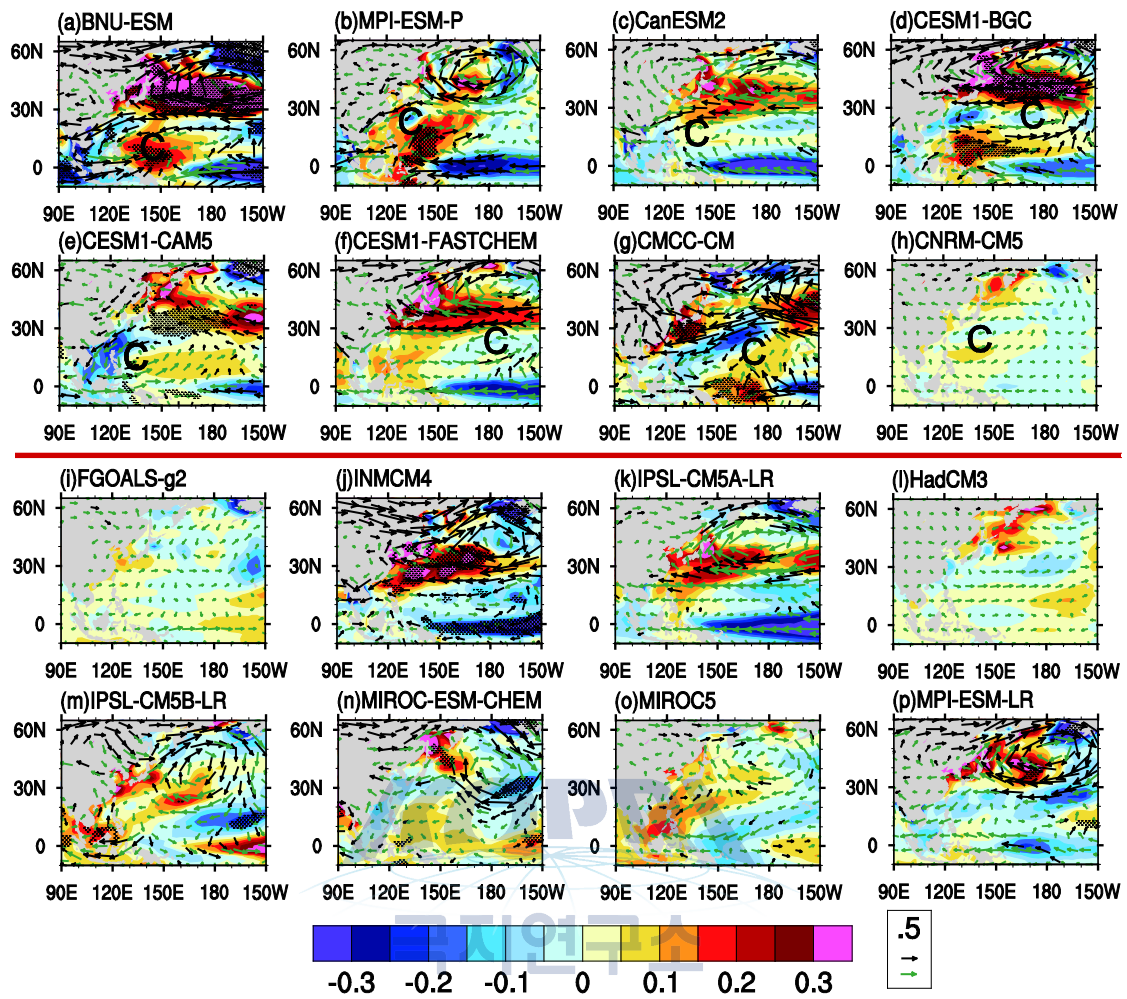


Fig. 2 Regressed MAM 850-hPa wind (green and black vectors: m/s) and SST (shadings: degree) anomalies against the spring AO index for the following models: (a) BNU-ESM, (b) MPI-ESM-P, (c) CanESM2, (d) CESM1-BGC, (e) CESM1-CAM5, (f) CESM1-FASTCHEM, (g) CMCC-CM, (h) CNRM-CM5, (i) FGOALS-g2, (j) INMCM4, (k) IPSL-CM5A-LR, (l) HadCM3, (m) IPSL-CM5B-LR, (n) MIROC-ESM-CHEM, (o) MIROC5 and (p) MPI-ESM-LR. The areas exceeding the 90% confidence level are dotted. The black vectors are statistically significant above 90% based on a t-test while the green vectors are not. The red line divides the models into two groups, and 'C' denotes the center of the cyclonic anomaly.

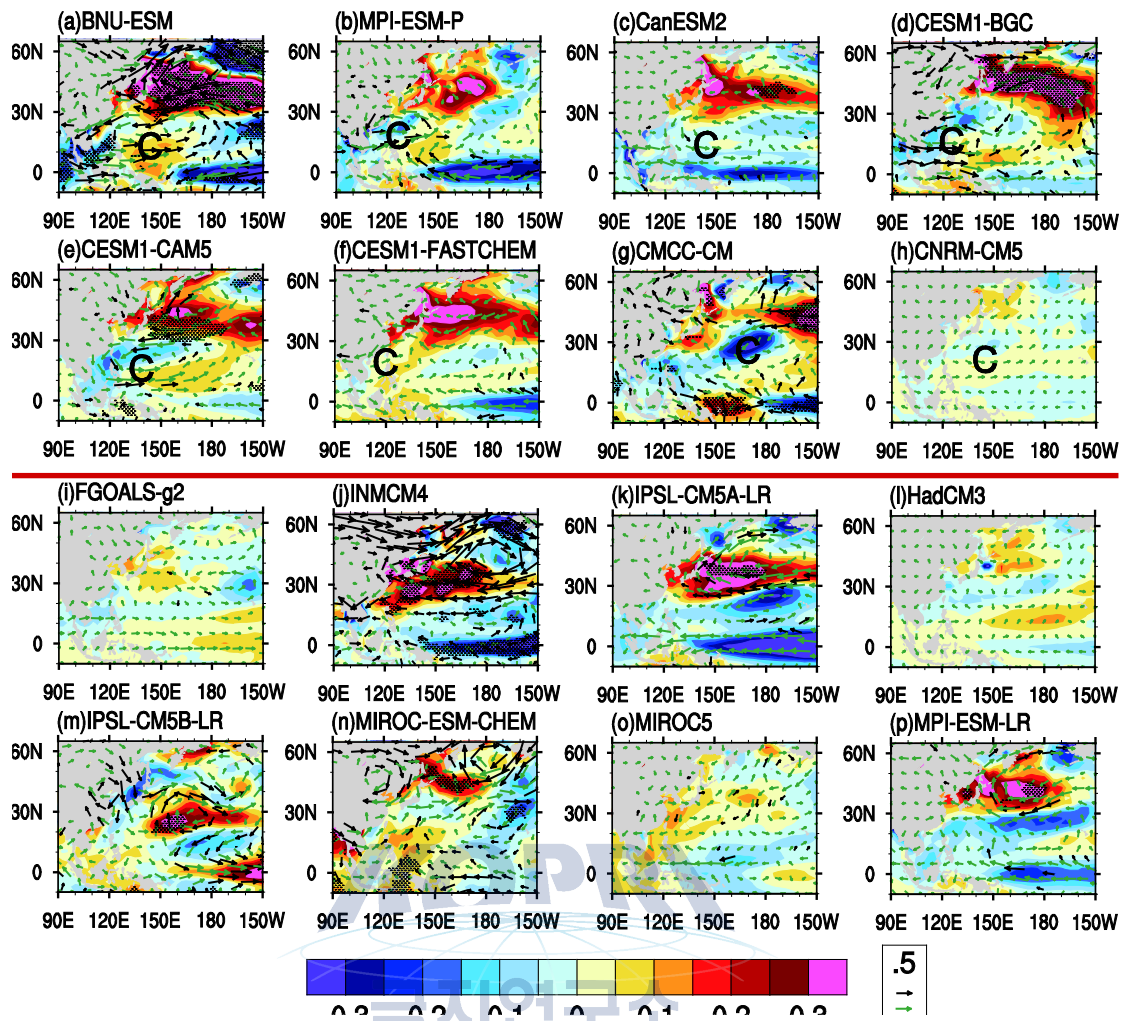


Fig. 3 Regressed MJJ 850-hPa wind (green and black vectors: m/s) and SST (shadings: degree) anomalies against the spring AO index for the following models: (a) BNU-ESM, (b) MPI-ESM-P, (c) CanESM2, (d) CESM1-BGC, (e) CESM1-CAM5, (f) CESM1-FASTCHEM, (g) CMCC-CM, (h) CNRM-CM5, (i) FGOALS-g2, (j) INMCM4, (k) IPSL-CM5A-LR, (l) HadCM3, (m) IPSL-CM5B-LR, (n) MIROC-ESM-CHEM, (o) MIROC5 and (p) MPI-ESM-LR. The areas exceeding the 90% confidence level are dotted. The black vectors are statistically significant above 90% based on a t-test while the green vectors are not. The red line divides the models into two groups, and 'C' denotes the center of the cyclonic anomaly.

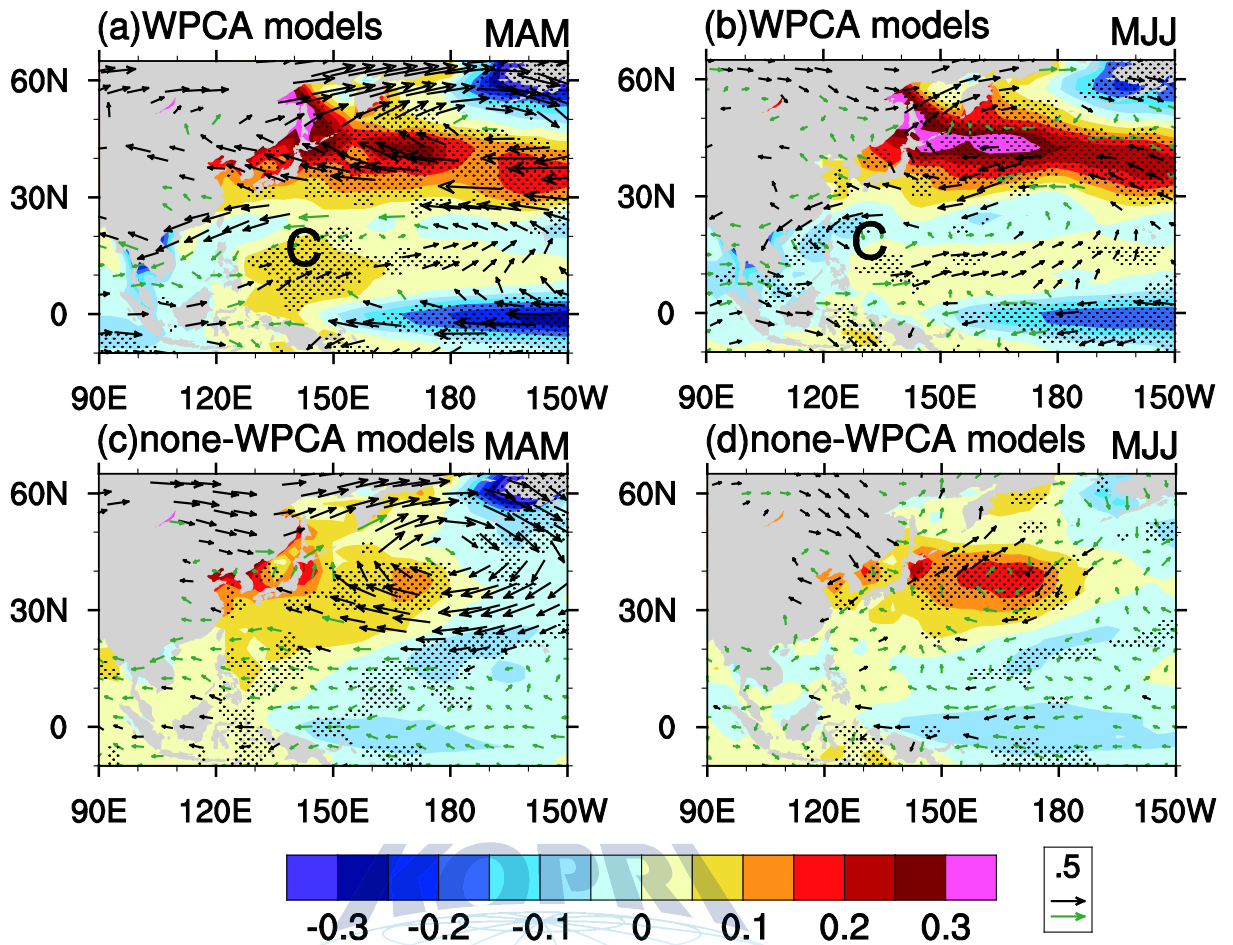


Fig. 4 Regressed 850-hPa wind (green and black vectors: m/s) and SST (shadings: degree) anomalies against the spring AO index for the MME of (a)/(b) the “WPCA” models and (c)/(d) the “non-WPCA” models, respectively, and for (a)/(c) MAM and (b)/(d) MJJ. ‘C’ denotes the center of the cyclonic anomaly. Dots and black vectors mean that more than 75% models show the same sign responses with the MME on the grids.

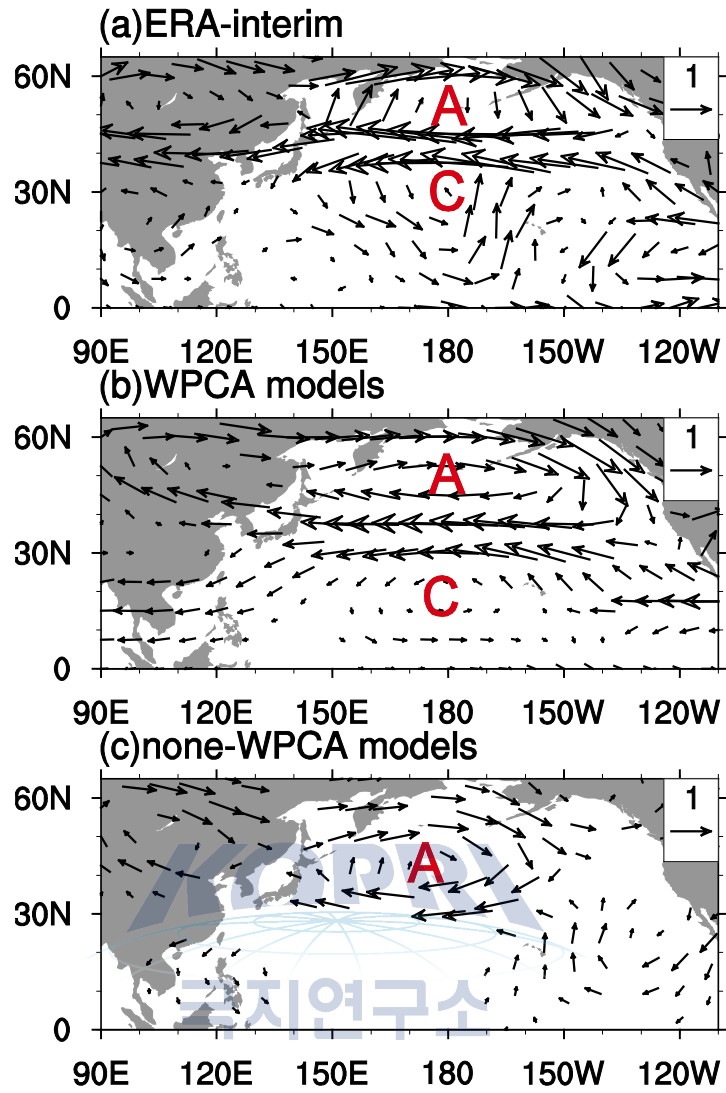


Fig. 5 Regressed MAM 300-hPa wind (m/s) anomalies against the spring AO index for (a) the ERA-interim reanalysis, (b) the MME of the “WPCA” models and (c) the MME of the “non-WPCA” models. The red ‘A’ and ‘C’ denote the centers of the anticyclonic and cyclonic anomalies, respectively. Only the wind vectors that exceed 0.2 m/s are plotted.

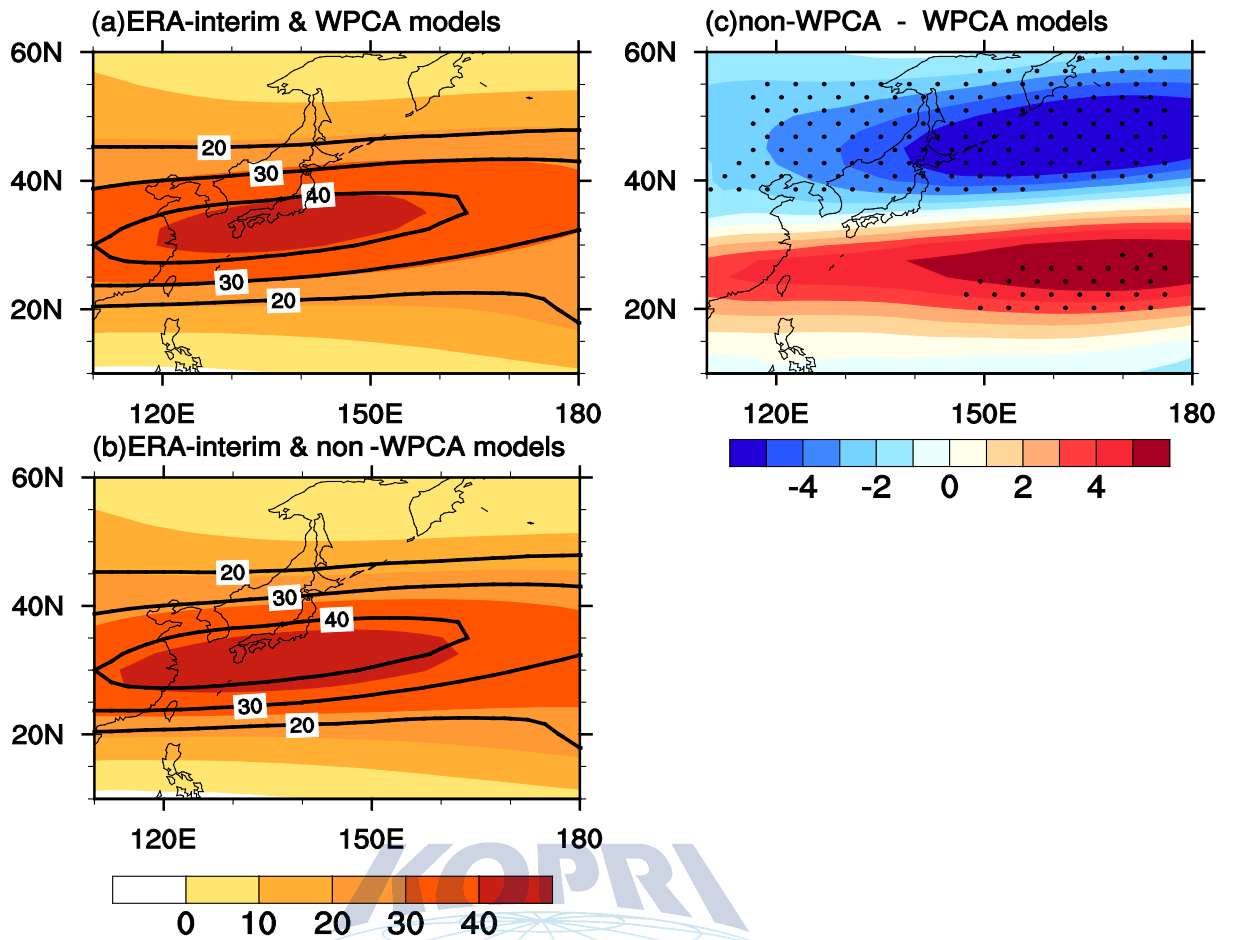


Fig. 6 Averaged 200-hPa MAM zonal winds (m/s) based on the ERA-interim reanalysis (contours), (a) the MME of the “WPCA” models, (b) the MME of the “non-WPCA” models (shadings) and (c) the differences between the MME of the “non-WPCA” models and the MME of the “WPCA” models (“non-WPCA”-“WPCA”). The areas exceeding 90% confidence level are dotted.

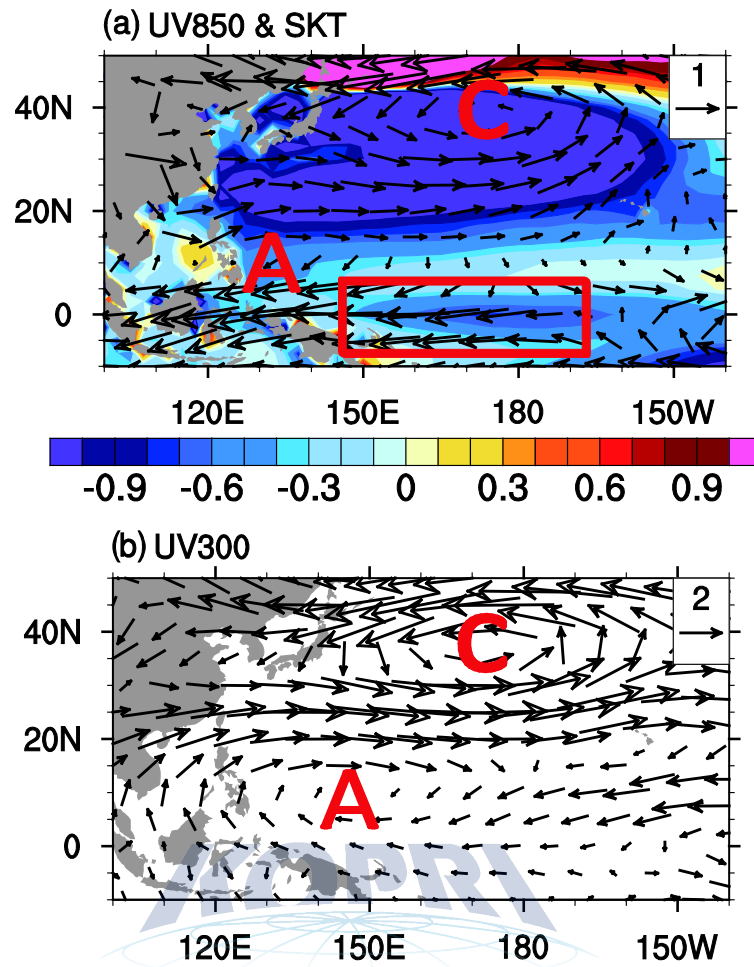


Fig. 7 Differences (a) in the simulated 850-hPa winds (vectors: m/s) and the mean skin temperature (shadings: degrees) and (b) in the simulated 300-hPa winds (vectors: m/s) between the MME of the “non-WPCA” models and the MME of the “WPCA” models in MAM (“non-WPCA”- “WPCA”). The red ‘A’ and ‘C’ denote the centers of the anticyclonic and cyclonic anomalies, respectively, and the red box indicates the important region.

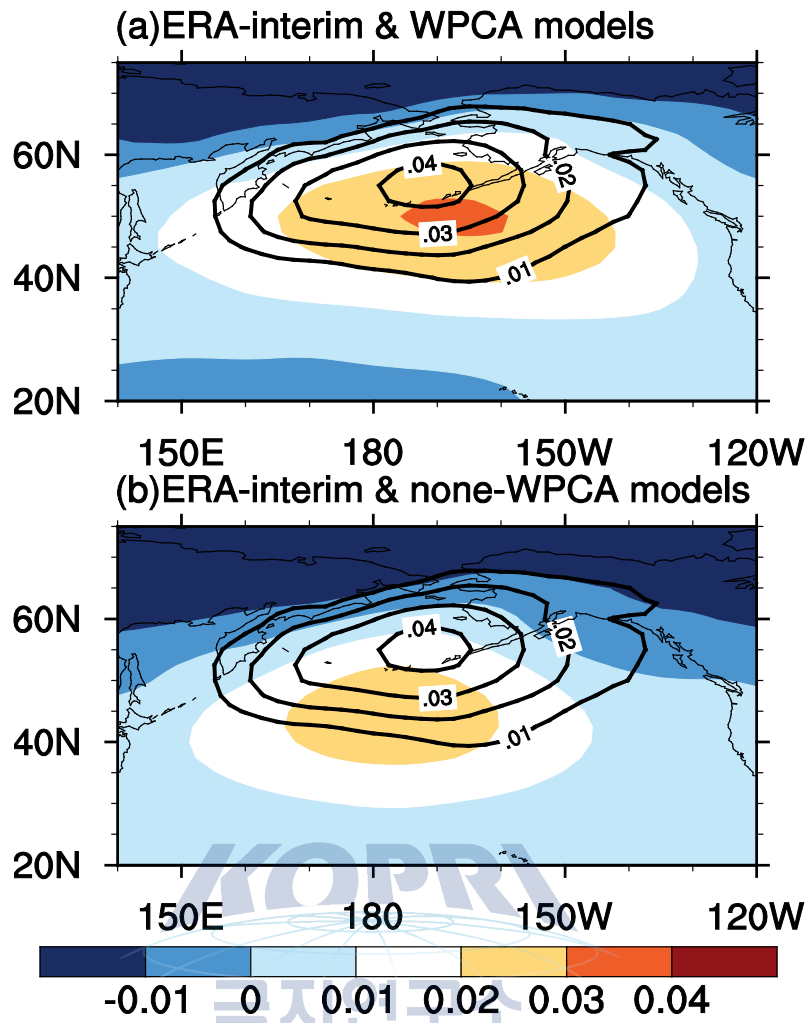


Fig. 8 The first leading mode of the MAM sea level pressure (hPa) based on the ERA-interim reanalysis (contours), (a) the MME of the “WPCA” models and (b) the MME of the “none-WPCA” models (shadings).

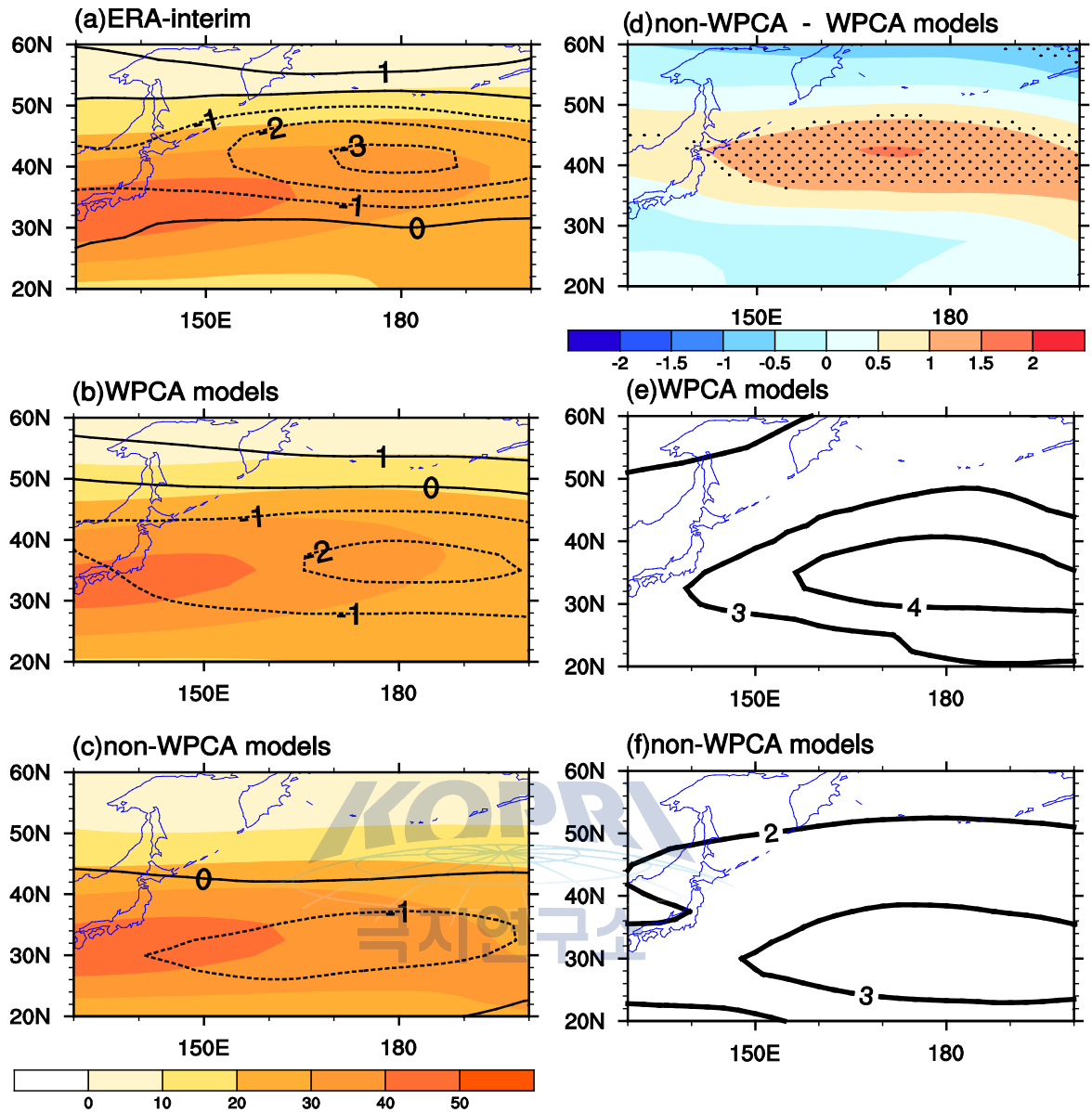


Fig. 9 Regressed 200-hPa zonal wind anomalies (contour: m/s) against the spring AO index and the 200-hPa MAM zonal winds (shadings: m/s) based on (a) the ERA-interim reanalysis, (b) the MME of the "WPCA" models, (c) the MME of the "non-WPCA" models, (d) the difference of the regressed 200-hPa zonal wind anomalies (contour: m/s) against the spring AO index between "WPCA" models and "non-WPCA" models and the standard deviation of the 200-hPa MAM horizontal winds in the (e) "WPCA" models and (f) "non-WPCA" models (contours: m/s). The areas exceeding 90% confidence level are dotted.

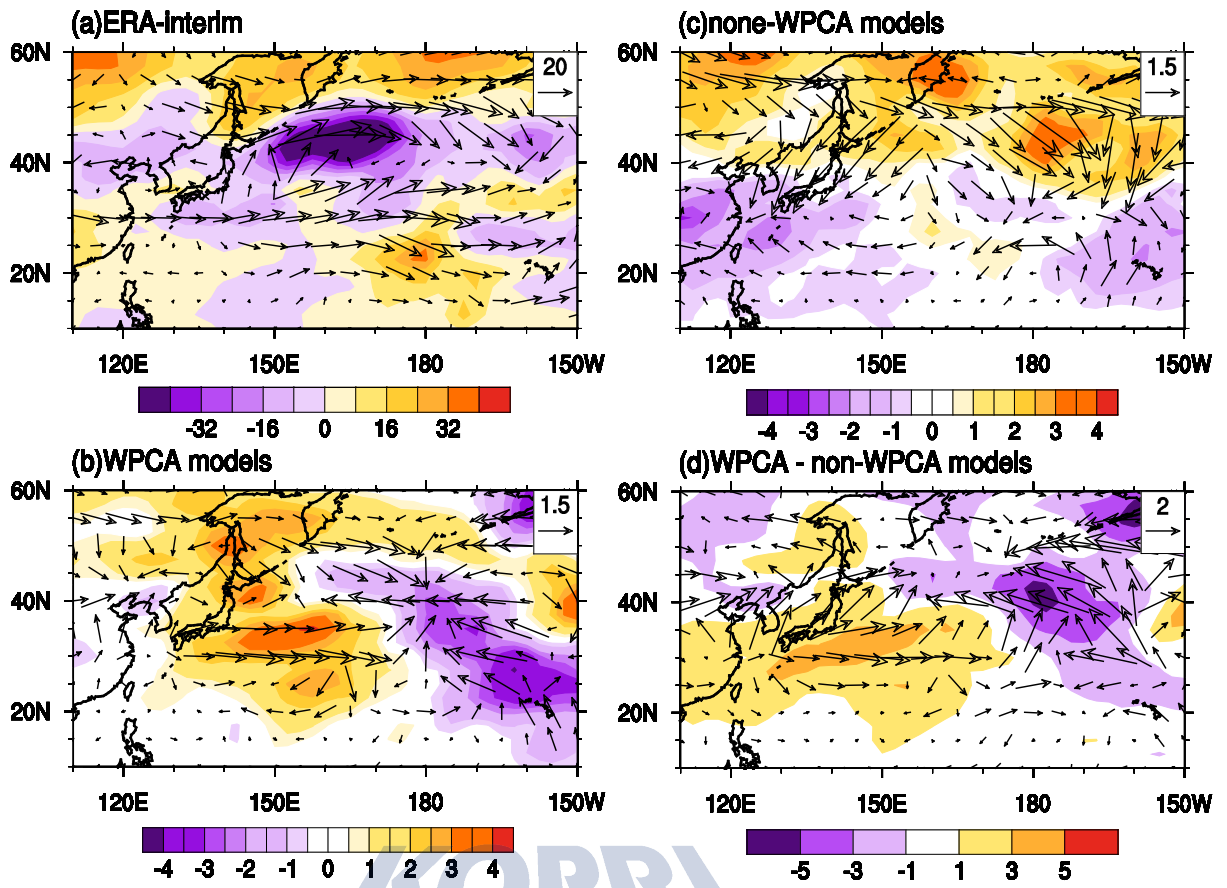


Fig. 10 Changes of MAM 200-hPa E-vectors (vector: m^2/s^2) and eddy kinetic energy (shadings: m^2/s^2) in association with the spring AO based on (a) the ERA-interim reanalysis, (b) the MME of the “WPCA” models, (c) the MME of the “non-WPCA” models and (d) the difference between two types of models (“WPCA” models – “non-WPCA” models).

5. *Related study funded by the KOPRI project: Causes of eastern Antarctica surface cooling related to ozone depletion during austral summer*

Motivation and goals:

The cooling trend over the EA surface through the early 2000s has been found to be consistent with the observed trend toward a high index polarity of the Southern Annular Mode (SAM) (e.g., Monaghan et al. 2008; Marshall et al., 2011), which has a close linkage with the Antarctic ozone hole (e.g., Gillett and Thompson, 2003; Fogt et al., 2009; Thompson et al., 2011). We have confidence in the linkage between the ozone depletion and surface-cooling trend over EA (Thompson et al., 2011), but we do not yet fully understand how the stratospheric ozone depletion causes the EA surface cooling. The stratospheric ozone depletion has two major effects on the troposphere and surface. The first is a radiative effect involving two contrasting processes: increased ultraviolet and visible radiation reaching the surface (e.g., Ramanathan and Dickinson, 1979), but reduced downward thermal infrared radiation to the surface (e.g., Grise et al., 2009), both of which determine the net adjusted radiative forcing reaching the surface. Is the net surface radiative forcing associated with the ozone hole negative or positive? The answer is uncertain (e.g., Hu et al., 2011; Previdi and Polvani, 2012). The other effect is a dynamical one, associated with circulation variation induced by ozone depletion. Related to ozone depletion, the most significant circulation variation is the enhanced circumpolar westerly jet (e.g., Gillett and Thompson, 2003). On the one hand, this strengthened westerly jet tends to isolate most of Antarctica and leads to a reduction in meridional advection of heat onto the continent, cooling the polar region (e.g., Thompson et al., 2000; Barnes and Hartmann, 2010); but on the other hand, the intensified westerly winds reduce the blocking effect of the Antarctic Peninsula, leading to a higher frequency of relatively warm air masses being advected eastward over the orographic barrier of the northern peninsula (Marshall et al., 2006). Therefore, how the ozone-hole-associated circulation change contributes to the surface cooling has yet to be clarified.

Due to the paucity of data over Antarctica, it is hard to quantify the effect of radiation (including clouds) and circulation from an observational perspective. Numerical model outputs have been considered to be a reasonable method to differentiate the contribution of the above-mentioned effects (radiation, cloud, and circulation) to surface temperature change (e.g., Qu et al., 2012). FGOALS-s2 (the second spectral version of the Flexible Global Ocean-Atmosphere-Land System model) is a newly released coupled general circulation model that participated in IPCC AR5 (Fifth Assessment Report). Through two sets of

numerical experiments, this study first evaluates the performance of the EA surface cooling in this model, and then investigates the relative quantitative contributions of radiation and circulation associated with ozone depletion to the EA surface cooling.

Work done and findings

In this study, we first evaluated the ability of FGOALS-s2 to simulate the surface climate change over the Antarctic, and found that the OH run (control) of FGOALS-s2 was able to reproduce the surface-cooling trend over the EA continent and strengthened circumpolar westerly flow in the past 30 years; however, the EA cooling amplitude was smaller than observed. Without the ozone hole, both the surface cooling and the intensified circumpolar westerly were remarkably weakened in the NOH simulation. Therefore, the effects of ozone depletion on enhancing the surface cooling and strengthening the westerly stream in the simulation were consistent with many previous studies.

Comparing the two numerical experiments, we further analyzed the surface budget change to investigate the causes of the EA surface cooling, and found that the surface radiation change acts as the dominant contributor to the EA cooling, which is much larger than the surface heat flux change. The surface radiation changes come from two effects associated with ozone depletion: the DRE (direct radiation effect) and the CRE (cloud radiation effect). The DRE and CRE cause comparable surface cooling over EA, although they have opposite effects when accompanied by ozone depletion. The DRE causes cooling because the decrease of downward LW radiation is larger than the increase of downward SW radiation, and the CRE causes cooling because the decreased downward SW radiation is larger than the increased downward LW radiation. In the final analysis, the CRE was actually found to be associated with a dynamical circulation effect. In this sense, the radiation effect and dynamical effect play comparable roles in the causes of surface cooling over EA.

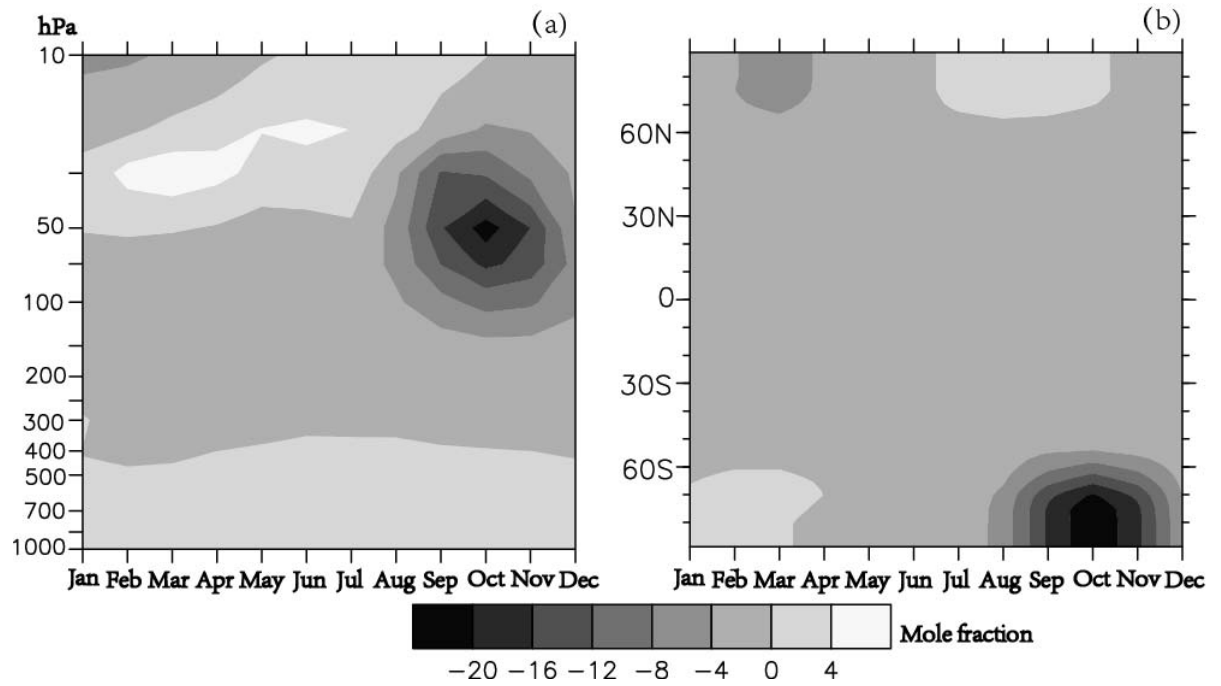


Fig. 1. The horizontal and vertical extents of the ozone hole (difference between climatology of 1976-2005 and 1975) used in this study based on the SPARC ozone datasets: (a) vertical extent over the polar cap averaged over the area south of 65°S by month; (b) zonal mean latitudinal crosssection at 50 hPa by month.



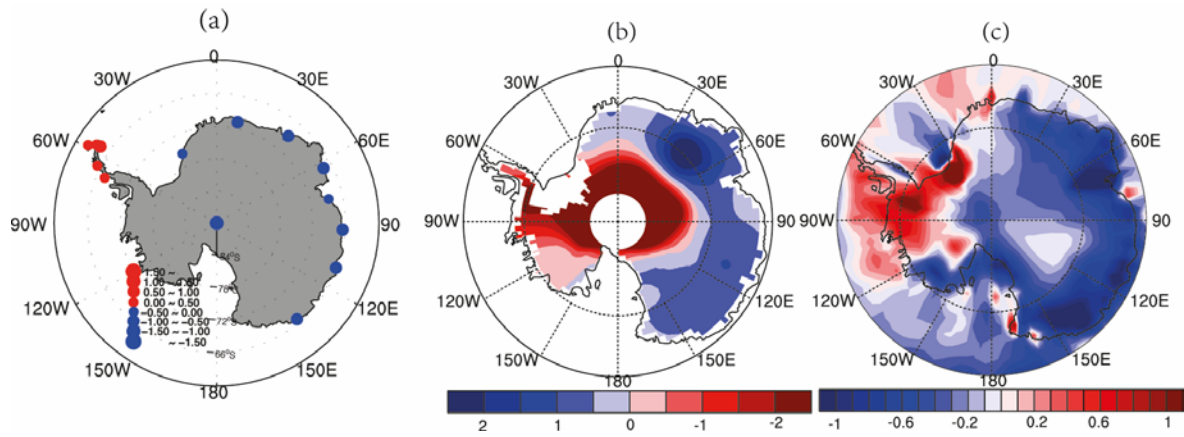


Fig. 2. Austral summer surface temperature trends [$\text{K} (10\text{yr})^{-1}$] from 1976 to 2005 retrieved from (a) Antarctica station data, (b) Delaware land data, and (c) ERA-interim reanalysis data.



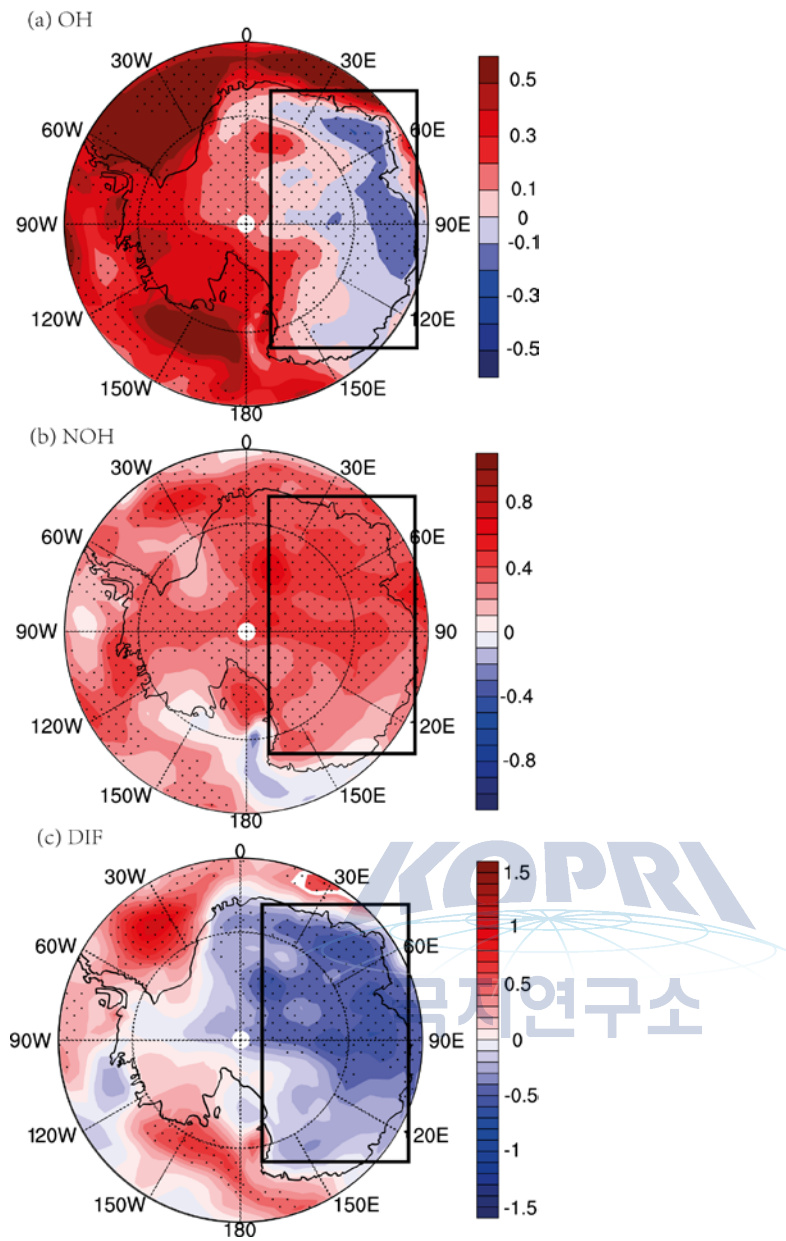


Fig. 3. Austral summer surface temperature trends [$\text{K} (10\text{yr})^{-1}$] from 1976 to 2005 for the (a) OH results, (b) NOH results, and (c) their difference (OH minus NOH). Dotted regions are above the 90% confidence level according to the Student's *t*-test.

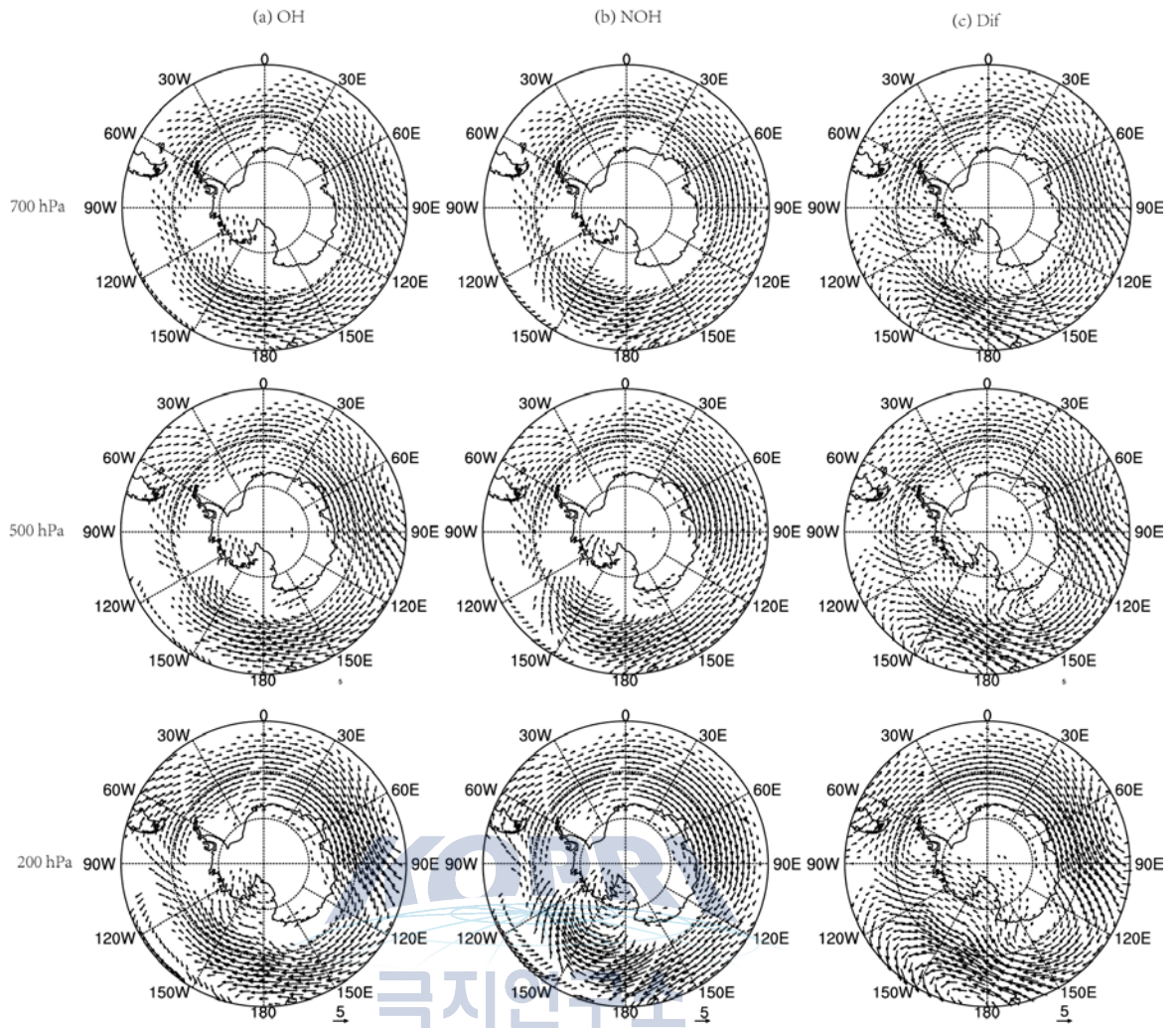


Fig. 4. Linearized trend of 700 hPa(upper row), 500 hPa(middle row), and 200 hPa(lower row) winds [$\text{m s}^{-1} (10\text{yr})^{-1}$] for the(a) OH run, (b) NOH run, and (c) their difference. Vectors are shown above the 90% confidence level.

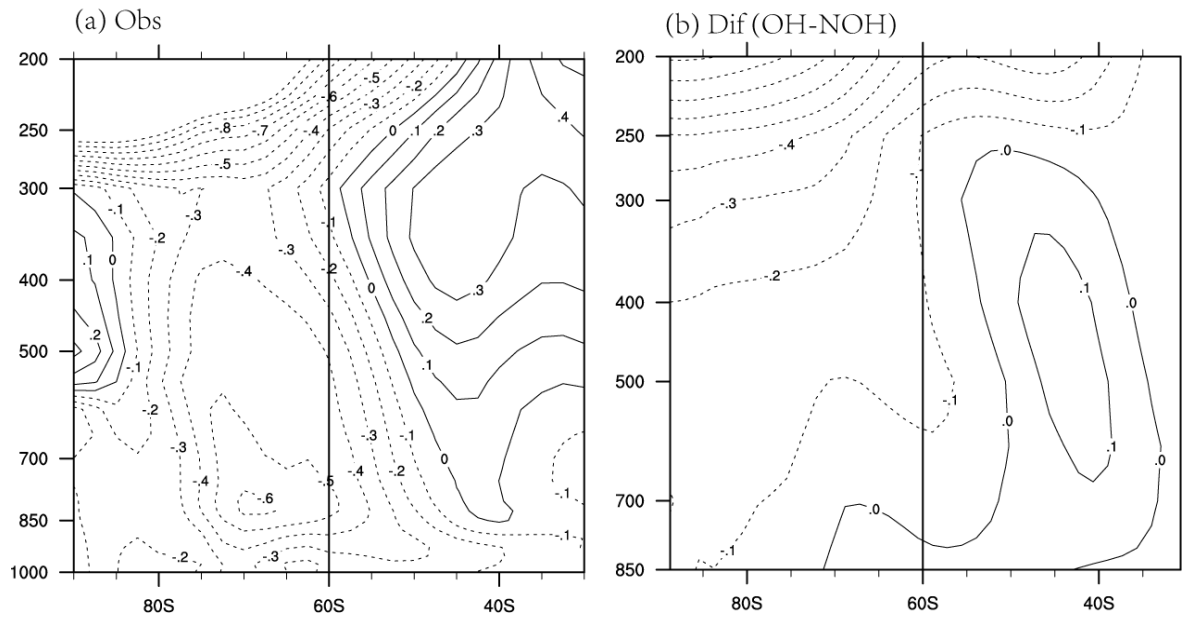


Fig. 5. Zonal mean austral summer temperature trend [$\text{K}(10\text{yr})^{-1}$] along with height (units: hPa) in (a) observation (ERA-interim) and (b) difference between the OH and NOH model runs.



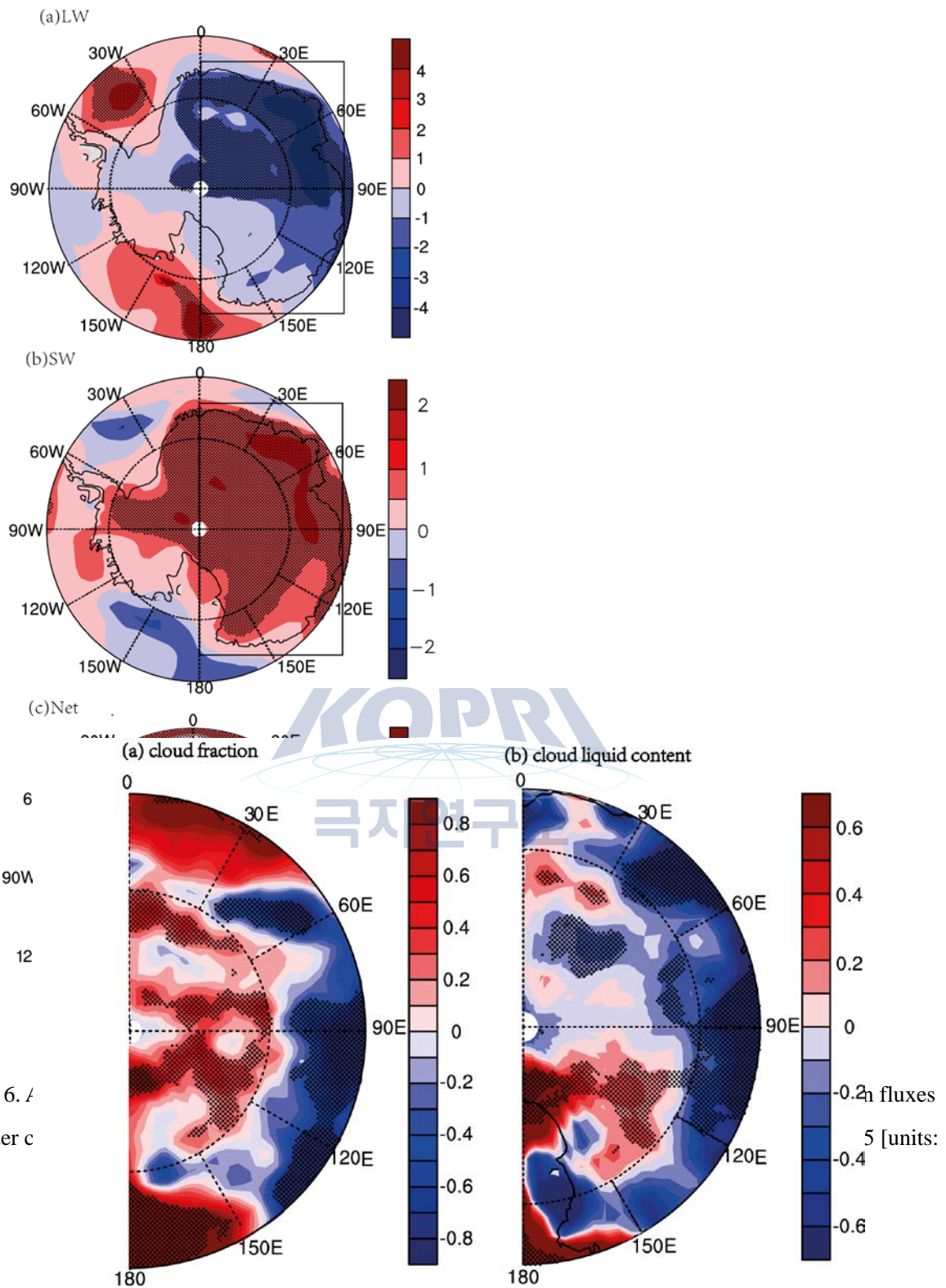


Fig. 6. *A*
(under c

Fig. 7. Austral summer tendency differences of cloud fraction and cloud liquid water mass fraction (calculated as the mass of cloud liquid water in the grid cell divided by the mass of air including the water in all phases in the grid cells) from 1976 to 2005 (units:100%).Dotted regions are above the 90% confidence level.

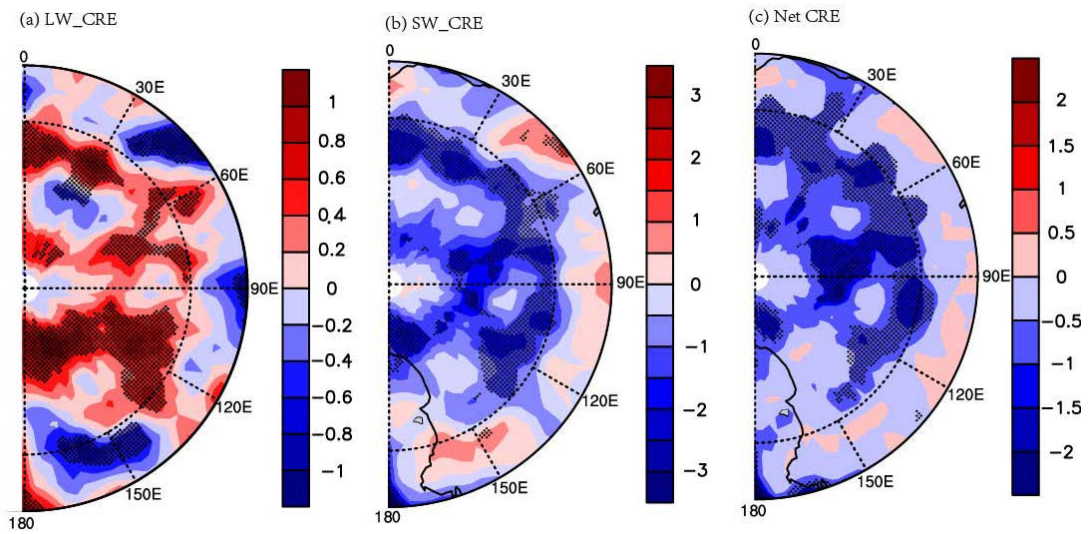


Fig. 8. Austral summer tendency differences of surface downward radiation fluxes caused by the CRE for (a) LW, (b) SW, and (c) net downward radiation (LW +SW) from 1976 to 2005 [units: $\text{Wm}^{-2} (10\text{yr})^{-1}$]. Dotted regions are above the 90% confidence level.

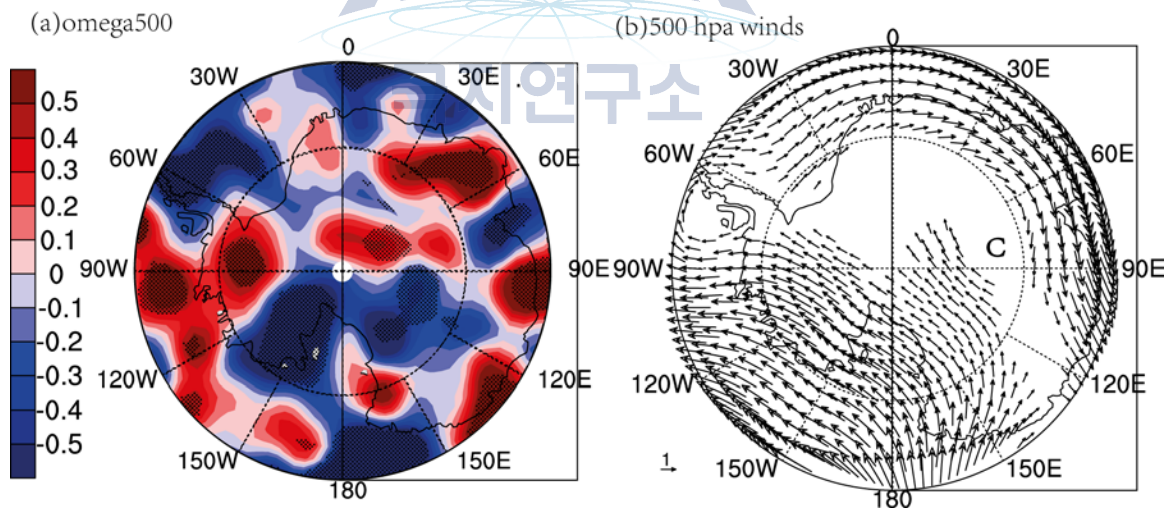


Fig. 9. Austral summer tendency differences of 500 hPa vertical velocity (down is positive) and 500 hPa winds [units: $\text{ms}^{-1} (10\text{yr})^{-1}$]. Dotted regions are above the 90% confidence level, and vectors shown are above the 90% confidence level.

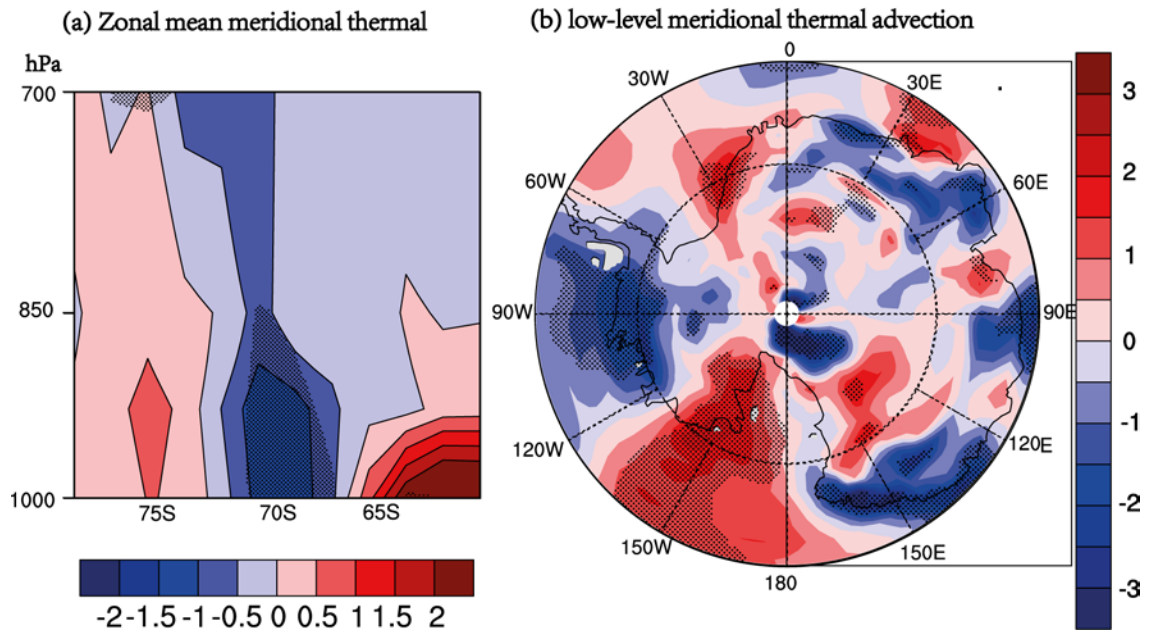


Fig. 10. (a) Zonal mean meridional thermal advection below 700 hPa; (b) low-level meridional thermal advection trend between 1000 hPa and 700 hPa. All the above are the austral summer tendency differences between the two experiments (OH minus NOH). Units are $\text{Ks}^{-1} (10\text{yr})^{-1}$. Dotted regions are above the 90% confidence level.



6. *Related study funded by the KOPRI project: To investigate the possible influences of atmospheric circulation patterns over the middle-high latitude upon the winter air quality in Beijing-Tianjin-Hebei district, northern China*

Motivation and goals

Beijing-Tianjin-Hebei (BTH) region is located in northern China, with approximately 110 million residents and 216,000 km² in size. As the rapid progress of urbanization and industrial development over the past three decades, the BTH region has become one of China's most economically developed regions and the third economic engine in China. However, the rapid economic growth and urbanization have increased the level of air pollution in recent decades. Many studies have focused on the physical and chemical properties of pollutants in Beijing and other cities (Feng et al., 2006; Yu et al., 2011; Xu et al., 2013; Zhao et al., 2013). And also studies demonstrated the influence of weather conditions or synoptic situations upon air pollutions (Zhao et al., 2009; Zhang et al., 2015). They elucidated clearly the formation and chemical composition of air pollutants and the dominant meteorological factors during heavy pollution in the BTH region. On the other hand, some studies demonstrated that the haze pollution occurring in the BTH region could be strongly affected by the local atmospheric circulations including sea-land and mountain-valley breeze circulations and the planetary boundary layer height (Lo et al., 2006; Liu et al., 2009; Chen et al., 2009; Miao et al., 2015). It is interesting to examine whether the winter haze pollution in BTH has been influenced by other known or unknown atmospheric circulations or teleconnections in the mid-high latitude of the Northern Hemisphere and whether there are some potential circulations that can be used for the forecast or evaluation of the winter haze pollution in BTH. To date, it is not clear about these questions. The main purpose of this study is to examine the possible relations between the atmospheric circulations and the winter haze pollution (the mean visibility and mean number of hazy days) over the BTH region and investigate the possible physical mechanism, which could be useful for a prediction of the winter haze pollution and could provide a scientific support to the government to take effective measures in advance to reduce or control the pollutant emission in case of an anomalous circulations leading to a serious haze pollution in the region.

Work done and findings

The variability of the winter haze pollutions (indicated by the mean visibility and number of hazy days) in Beijing-Tianjin-Hebei (BTH) region during the period 1981 to 2015 and its relationship to the atmospheric circulations in middle-high latitude were analyzed in this study. The winter haze pollution in BTH had distinct inter-annual and inter-decadal variabilities without a significant long-term trend. According to the spatial distribution of correlation coefficients, six atmospheric circulation indices (I_1 to I_6) were defined from the key areas in sea level pressure (SLP), zonal and meridional winds at 850 hPa (U850, V850), geopotential height field at 500 hPa (H500), zonal wind at 200 hPa (U200), and air temperature at 200 hPa (T200), respectively. All of the six indices have significant and stable correlations with the winter visibility and number of hazy days in BTH. In the raw (unfiltered) correlations, the correlation coefficients between the six indices and the winter visibility (number of hazy days) varied from 0.57 (0.47) to 0.76 (0.6) with an average of 0.65 (0.54); in the high-frequency (<10 yr) correlations, the coefficients varied from 0.62 (0.58) to 0.8 (0.69) with an average of 0.69 (0.64). The six circulation indices together can explain 77.7% (78.7%) and 61.7% (69.1%) variances of the winter visibility and number of hazy days in the year-to-year (inter-annual) variability, respectively. The increase of I_c (a comprehensive index derived from the six individual circulation indices) can cause a shallowing of the East Asian trough at the middle troposphere and a weakening of the Siberian high pressure field at sea level, and then accompanied by a reduction (increase) of horizontal advection and vertical convection (relative humidity) in the lowest troposphere and a reduced boundary layer height in BTH and its neighboring areas, which are favorable for the formation of haze pollutions in BTH winter, and vice versa. The high level of the prediction statistics and the reasonable mechanism suggested that the winter haze pollutions in BTH can be forecasted or estimated credibly based on the optimized atmospheric circulation indices. Thus it is helpful for government decision-making departments to take actions in advance in dealing with probably severe haze pollutions in BTH indicated by the atmospheric circulation conditions.

Table 1 Correlation coefficients of visibility and hazy days and circulation indices

		AO	NAO	PNA	EU	WP	SBH
Visibility	<i>r</i> 1	-0.11	0.00	0.16	0.61**	0.40*	0.39*
	<i>r</i> 2	0.05	0.22	0.16	0.71**	0.37*	0.36*
Number of hazy days	<i>r</i> 1	0.13	0.13	-0.10	-0.51**	-0.47**	-0.32
	<i>r</i> 2	-0.01	-0.11	-0.10	-0.70**	-0.56**	-0.37*

** Significant at the 0.01 level, * Significant at the 0.05 level. The *r*1 and *r*2 terms indicate the raw correlation and high-frequency (<10yr) correlation, respectively.

Table 2 List of the definition for the six circulation indices

Index	Variable	Expression
I ₁	SLP	SLP (38~50N, 84~108E) – SLP (36~52N, 126~150E; 24~40N, 150~184E)
I ₂	U _{850hPa}	U ₈₅₀ (55~75N, 40~110E) – U ₈₅₀ (40~50N, 45~75E)
I ₃	V _{850hPa}	V ₈₅₀ (32~64N, 104~120E)
I ₄	H _{500hPa}	H ₅₀₀ (46~64N, 50~92E) – H ₅₀₀ (28~44N, 16~28E; 28~42N, 120~156E)
I ₅	U _{200hPa}	U ₂₀₀ (42~52N, 60~110E) – U ₂₀₀ (64~76N, 50~96E; 28~36N, 120~152E)
I ₆	T _{200hPa}	T ₂₀₀ (46~66N, 146~196E)

Table 3 Correlation coefficients of visibility and number of hazy days and circulation indices

		I ₁	I ₂	I ₃	I ₄	I ₅	I ₆
Visibility	<i>r</i> 1	0.73**	0.57**	-0.76**	0.62**	-0.59**	-0.61**
	<i>r</i> 2	0.70**	0.68**	-0.80**	0.72**	-0.62**	-0.62**
Number of hazy days	<i>r</i> 1	-0.60**	-0.47**	0.60**	-0.47**	0.52**	0.60**
	<i>r</i> 2	-0.61**	-0.65**	0.69**	-0.67**	0.58**	0.64**

Same as Table 1

Table 4 List of the statistics for the Leave-N-out cross-validation estimations

N	Period covering	Visibility			Number of hazy days		
		r^2 (%)	SE	RE	r^2 (%)	SE	RE
1	1981-2015	62.7	0.74	0.61	41.5	3.37	0.38
	1981-2008	87.1	0.42	0.87	53.9	2.56	0.52
3	1981-2015	56.8	0.80	0.54	34.3	3.57	0.28
	1981-2008	86.8	0.42	0.87	52.6	2.59	0.51
5	1981-2015	59.2	0.78	0.57	35.3	3.54	0.30
	1981-2008	86.8	0.42	0.87	46.7	2.75	0.43
7	1981-2015	59.0	0.78	0.56	37.5	3.48	0.33
	1981-2008	86.4	0.43	0.86	44.7	2.80	0.41
9	1981-2015	56.2	0.80	0.54	32.5	3.62	0.27
	1981-2008	84.2	0.46	0.84	40.8	2.90	0.36
11	1981-2015	52.5	0.84	0.49	31.1	3.66	0.23
	1981-2008	84.4	0.46	0.84	48.2	2.71	0.44

(N denotes the number of sample removed in the cross-validation regressions; only the odd numbers of N were listed for short)



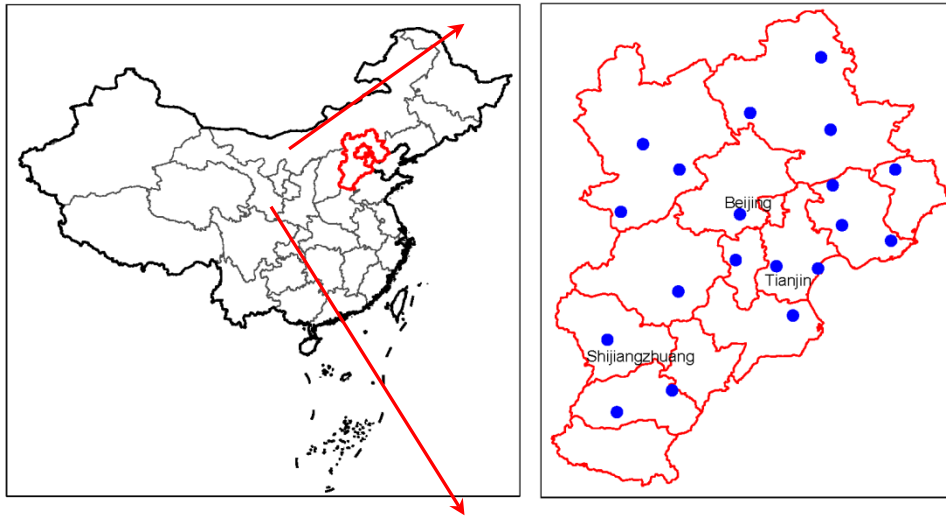


Figure 1 Research area and locations of the 19 synoptic meteorological stations

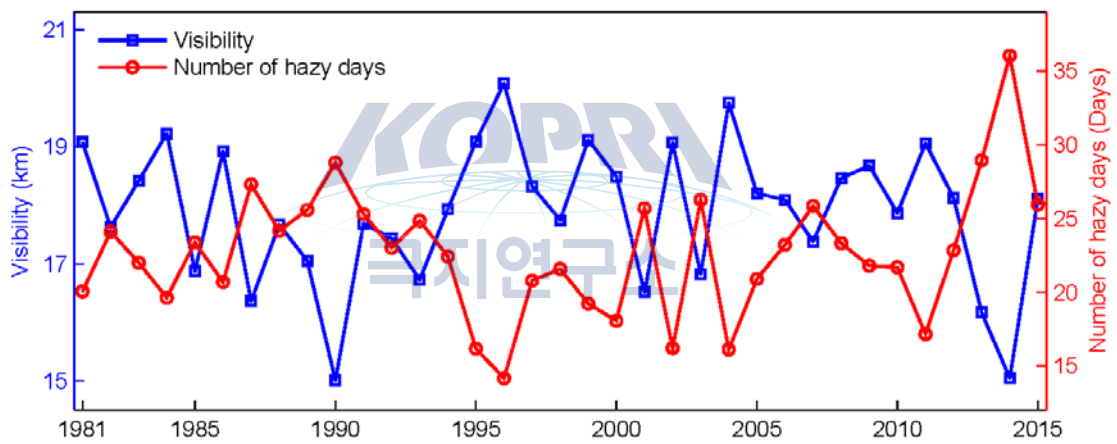


Figure 2 Curves of the winter mean visibility and number of hazy days in BTH

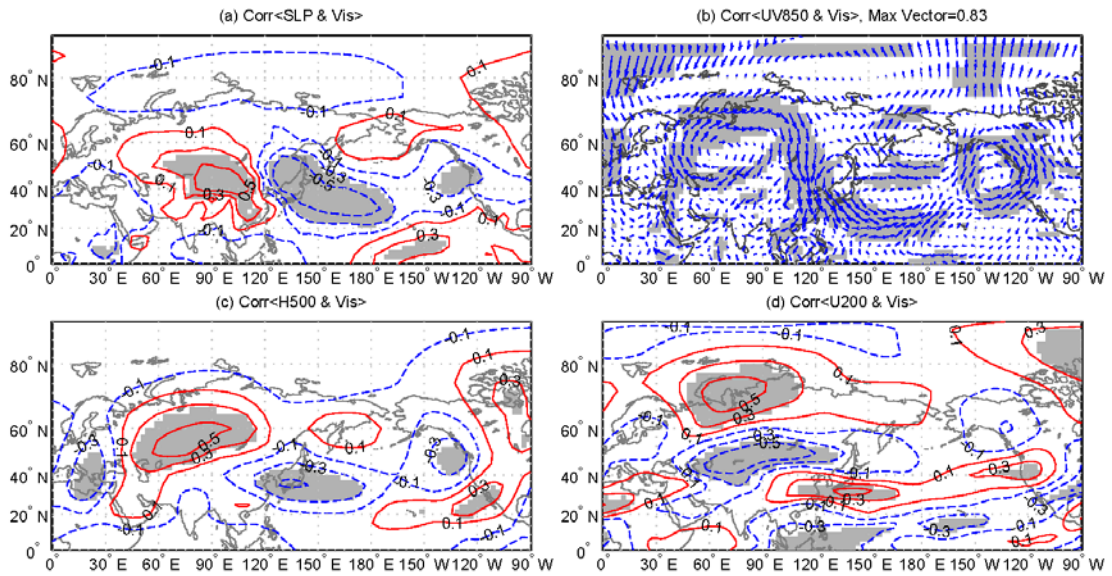


Figure 3, Spatial distribution of correlation coefficients between visibility and SLP (a), UV850 (b), H500 (c) and U200 (d) (Area significant at the 0.05 level are shaded; either U850 or V850 significant at the 0.05 level are shaded in b)

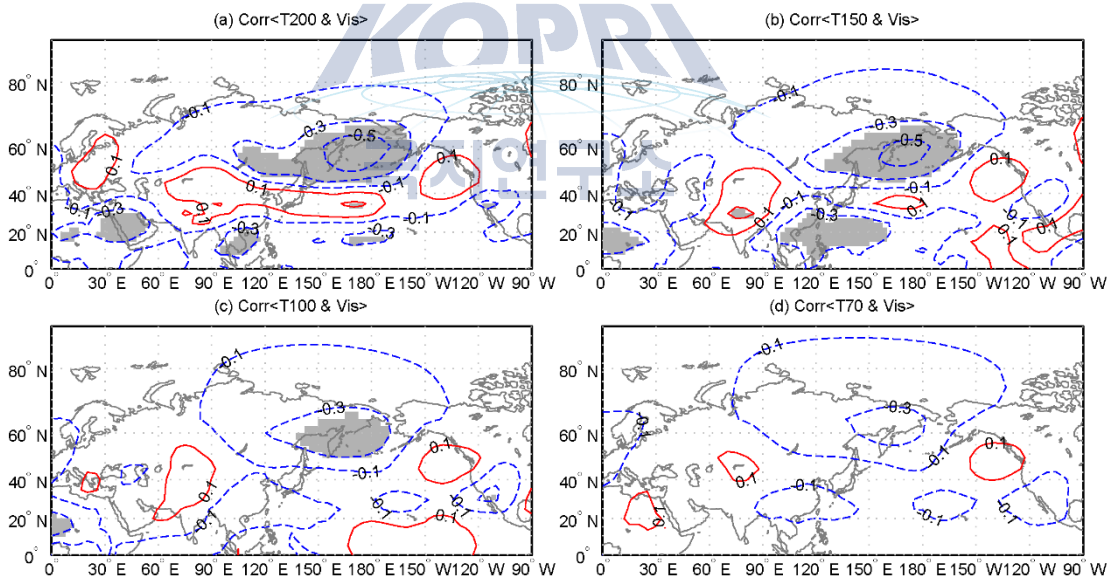


Figure 4 Spatial distribution of correlation coefficients between visibility and T200 (a), T150 (b), T100 (c) and T70 (d) (Area significant at the 0.05 level are shaded)

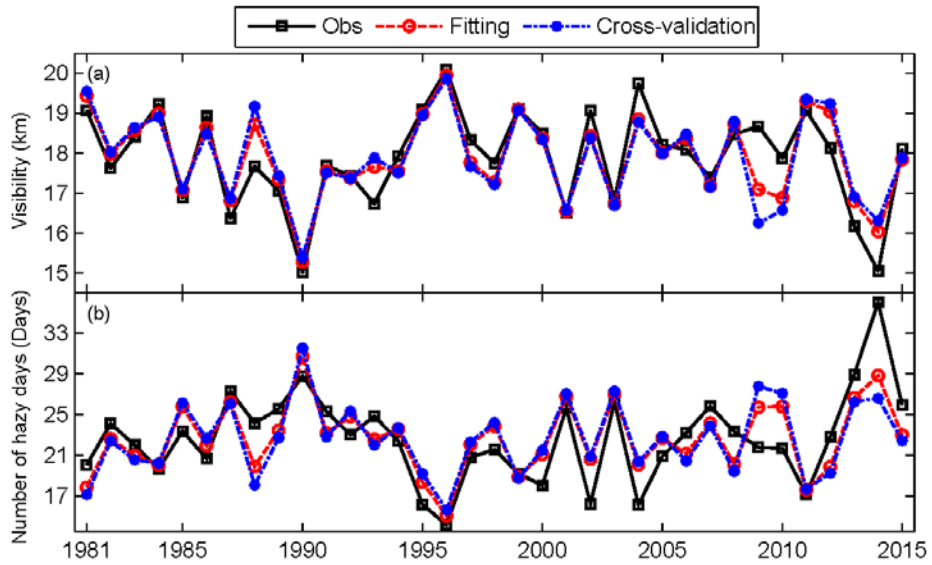


Figure 5 Curves of the observed and the predicted winter visibility (a) and number of hazy days (b) in the BTH region since 1981

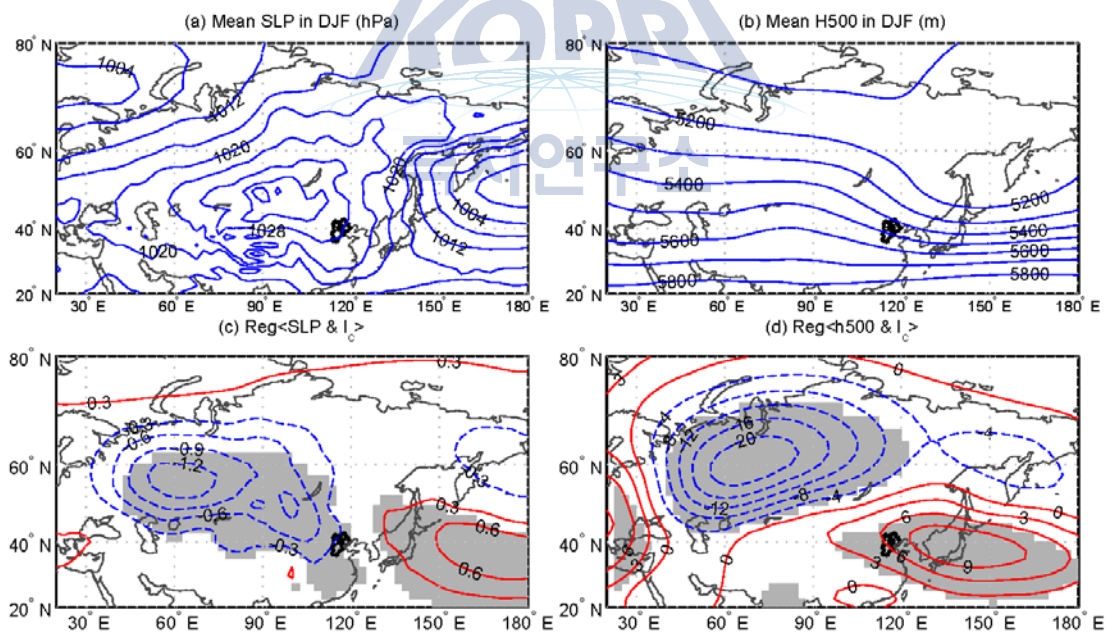


Figure 6 The climatological mean fields of SLP (a) and H500 (b) averaged in winter 1981 to 2010, and the spatial distribution of the regression coefficients of SLP (c) and H500 (d) upon the I_c over the period 1981 to 2015 (Area significant at the 0.05 level are shaded)

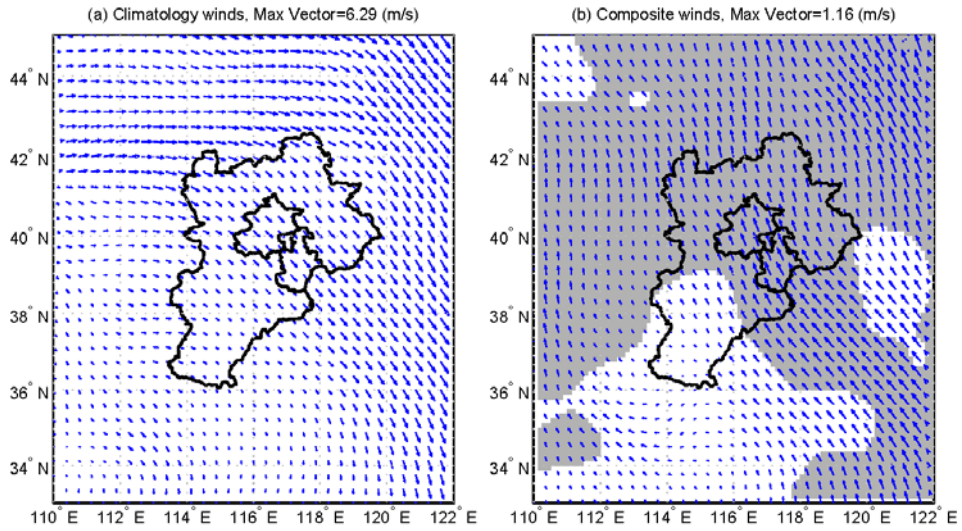


Figure 7 The climatological mean (a) and the composite (b) wind fields averaged from 1000 to 900 hPa
(Area significant at the 0.05 level are shaded)

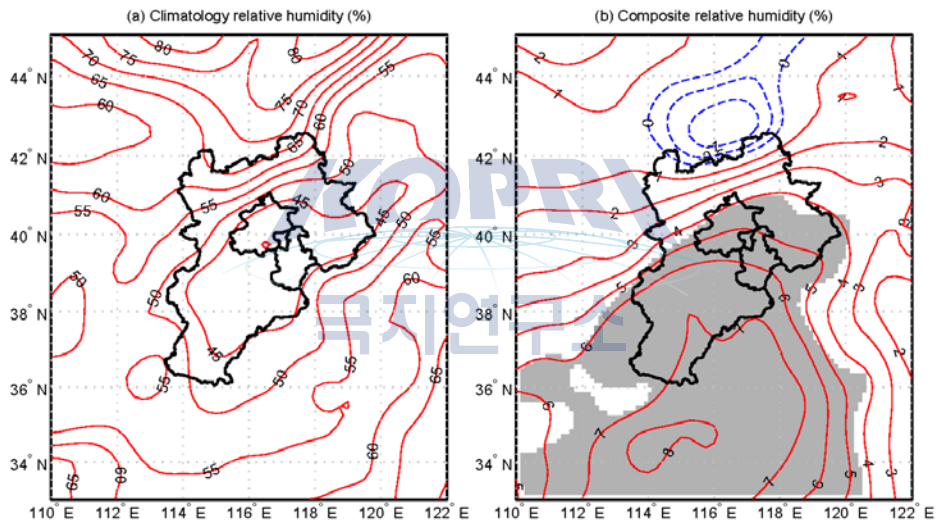


Figure 8 Same as Figure 7, but for relative humidity

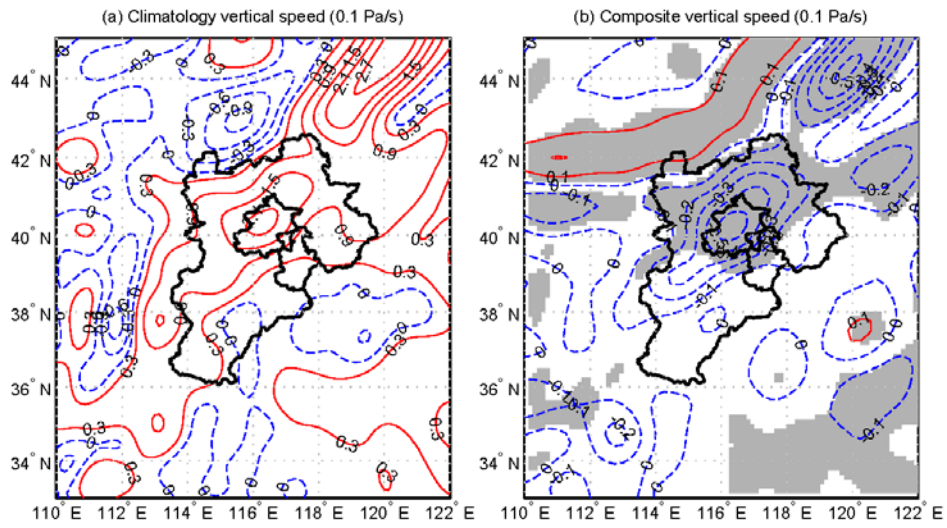


Figure 9 Same as Figure 7, but for vertical speed

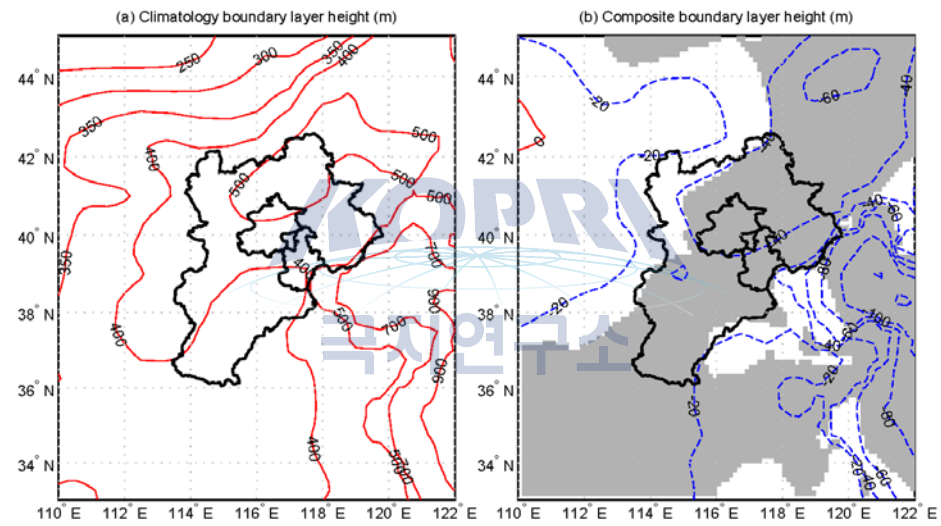


Figure 10 The climatological mean (a) and the composite (b) boundary layer height
(Area significant at the 0.05 level are shaded)

7. *Related study funded by the KOPRI project: To investigate the Evolution of surface O₃ and PM_{2.5} concentrations and their relationships with meteorological conditions over the last decade in Beijing*

Motivation and goals

Beijing is the capital and one of the largest cities of China, with approximately 20 million residents. The rapid economic growth and urbanization have increased the level of air pollution in recent decades (Streets et al., 2007; Chan and Yao, 2008). Beijing and northern China have frequently suffered from severe haze or smog days in recent years. Weather conditions play an essential role in the daily fluctuation of air pollutant concentrations. However, few studies have quantitatively explored the relationships between air pollutant concentrations and meteorological conditions for long time periods in Beijing.

Ozone (O₃) and fine particulate matter (PM_{2.5}) are the two major urban air pollutants in most of the cities, especially PM_{2.5} in Chinese cities, and they are of great concern because of their adverse effects to public health, visibility, vegetation and other pollution problems (Carlo et al., 20007; Hyslop, 2009; Fann et al., 2012). These pollutants are indicators for air quality and can be easily understood by the non-scientific community. In addition, O₃ and PM_{2.5} provide continuous and long-term pollutant data, especially the hourly O₃ and PM_{2.5} and meteorological datasets since 2005 (2006 for O₃) from two stations in Beijing. Generally, it is feasible and necessary to further re-examine the general characteristics of the evolution of O₃ and PM_{2.5} concentrations and their relationships with meteorological conditions over last decade in Beijing. Therefore, the goal of this study is to examine (i) the long-term trends of O₃ and PM_{2.5} concentrations over the last decade; (ii) the quantitative links between the variability of pollutant concentrations and meteorological variables on the synoptic timescale; (iii) the differences between the concentrations on haze days and non-haze days and in urban and rural areas.

Work done and findings

In this study, hourly and daily records since 2005 and correlation, regression and composite methods were used to analyze the long-term evolution of surface O₃ and PM_{2.5} concentrations at the rural station of Shangdianzi (SDZ) and urban station of Baolian (BL) over Beijing and their relationships with meteorological conditions. The results show that the mean concentrations of PM_{2.5} (O₃) decreased (increased) at the urban and rural stations over the last decade. The linear trends of the annual mean concentrations of PM_{2.5} at BL and SDZ were -31.8 ug/m³/10yr (-4.3 %/yr) (p<0.01) and -13.3 ug/m³/10yr

(-2.9 %/yr) ($p < 0.05$), respectively. In winter, the mean wind speed (W_s) and relative humidity (RH) were the most closely correlated with O_3 at both stations, whereas RH and sunshine hours (S) were most closely correlated with $PM_{2.5}$. The correlation coefficients and explained variances in spring and autumn were generally less than those in winter and greater than those in summer. Moreover, increase in precipitation can significantly reduce the $PM_{2.5}$ concentration in both urban and rural areas in Beijing, whereas trace and light precipitation more effectively decrease the O_3 concentration. Concentrations of $PM_{2.5}$ (O_3) on haze days increased by 114% (3%) and 162% (20%) compared with that on non-haze days at the urban and rural stations, respectively. This result suggests that haze is a major manifestation of air pollution in Beijing.



Table 1. Linear trends of concentrations over the period 2005-2013
(unit is $\mu\text{g}/\text{m}^3/10\text{yr}$, the values in brackets are the trend magnitude in unit of $\%/yr$)

		annual	winter	spring	summer	autumn
$\text{O}_3^{\#}$	BL	1.8[0.8]	-1.1[-1.4]	4.3[1.7]	3.2[0.8]	-1.8[-1.3]
	SDZ	3.5[1.0]	-0.7[-0.4]	8.0[1.9]	7.4[1.4]	-2.2[-1.3]
$\text{PM}_{2.5}$	BL	-31.8[-4.3]**	-15.7[-2.0]	-31.4[-4.6]*	-29.9[-4.1]**	-50.6[-6.7]**
	SDZ	-13.3[-2.9]*	8.0[2.4]	-26.1[-5.8]*	-16.9[-3.3]*	-5.9[-1.1]

** $p < 0.01$, * $p < 0.05$, based on a two-tailed Student's t-test; # the period is 2006-2013 for O_3 .

Table 2. Correlation coefficients of the daily O_3 concentration and meteorological factors in different seasons

		W_s	W_d	T	RH	P	R	S
Winter	SDZ	0.60[0.61]	-0.29[-0.34]	-0.09[-0.05]	-0.56[-0.62]	0.27[0.39]	-0.11[-0.14]	0.45[0.48]
	BL	0.62[0.71]	0.35[0.37]	-0.02[0.10]	-0.53[-0.59]	0.14[0.27]	-0.06[-0.04]	0.46[0.47]
Spring	SDZ	0.12[0.23]	0.09[-0.03]	0.65[0.34]	-0.06[-0.20]	-0.35[0.00]	-0.03[-0.11]	0.27[0.22]
	BL	0.13[0.43]	0.09[0.16]	0.54[0.27]	-0.12[-0.37]	-0.30[0.12]	0.01[-0.10]	0.31[0.44]
Summer	SDZ	0.37[0.28]	0.30[0.29]	0.27[0.35]	-0.25[-0.11]	-0.10[-0.08]	-0.11[-0.09]	0.04[0.08]
	BL	0.14[0.14]	0.12[0.04]	0.41[0.51]	-0.42[-0.42]	-0.08[-0.07]	-0.22[-0.21]	0.44[0.50]
Autumn	SDZ	0.11[0.22]	0.21[0.11]	0.60[0.34]	0.20[-0.01]	-0.39[-0.08]	0.06[-0.05]	0.16[0.07]
	BL	0.19[0.41]	0.09[0.16]	0.62[0.32]	-0.08[-0.34]	-0.45[-0.04]	0.01[-0.03]	0.32[0.38]

(SDZ and BL indicate the stations of Shangdianzi and Baolian, respectively. W_s , W_d , T , RH , P , R and S denote the mean wind speed, daily wind direction of the maximum wind speed, daily mean temperature, relative humidity, surface pressure, the daily precipitation amount and sunshine hours, respectively. The values in brackets denote the high frequency (<10 days) correlations. The numbers of samples are much greater than 100 for all correlations, so the correlation coefficients for the confidence levels of 0.05 and 0.01 are ± 0.20 and ± 0.25 , respectively; the significance values at $p < 0.05$ are shaded.)

Table 3. Correlation coefficients of the daily $\text{PM}_{2.5}$ concentration and meteorological factors in different seasons

		W_s	W_d	T	RH	P	R	S
Winter	SDZ	-0.39[-0.35]	0.34[0.26]	0.42[0.34]	0.65[0.50]	-0.43[-0.38]	0.12[-0.03]	-0.57[-0.52]
	BL	-0.44[-0.41]	-0.30[-0.21]	0.23[0.21]	0.66[0.49]	-0.33[-0.42]	0.03[-0.03]	-0.50[-0.43]
Spring	SDZ	0.01[-0.07]	0.33[0.29]	0.26[0.31]	0.35[0.43]	-0.34[-0.41]	-0.01[-0.01]	-0.36[-0.41]
	BL	-0.28[-0.39]	-0.23[-0.18]	0.23[0.24]	0.35[0.42]	-0.37[-0.48]	-0.04[-0.04]	-0.23[-0.30]
Summer	SDZ	-0.02[-0.09]	0.35[0.28]	0.26[0.34]	0.24[0.33]	0.03[-0.05]	-0.03[-0.05]	-0.40[-0.44]
	BL	0.02[-0.12]	0.00[0.01]	0.26[0.33]	0.13[0.24]	-0.07[-0.17]	-0.06[-0.04]	-0.10[-0.34]
Autumn	SDZ	-0.25[-0.29]	0.33[0.26]	0.16[0.29]	0.43[0.58]	-0.24[-0.42]	-0.05[-0.03]	-0.38[-0.41]
	BL	-0.17[-0.27]	-0.17[-0.12]	-0.02[0.07]	0.41[0.58]	-0.11[-0.34]	-0.11[-0.07]	-0.28[-0.37]

(Same as Table 2)

Table 4. Explained variances of the seven meteorological factors upon the daily variability of O₃ and PM_{2.5} in the different seasons

		Winter	Spring	Summer	Autumn
O ₃	SDZ	52%	48.1%	29.2%	41.0%
	BL	45%	38.0%	29.3%	50%
PM _{2.5}	SDZ	59%	34.8%	37.5%	32.3%
	BL	50%	28.8%	22.8%	29.1%



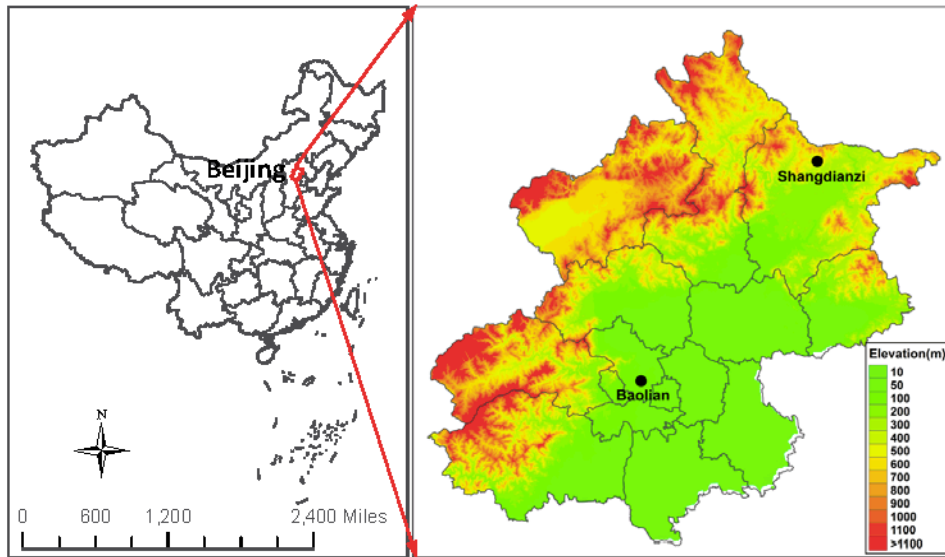


Fig. 1. Locations of the urban station of Baolian (BL) and rural station of Shangdianzi (SDZ)

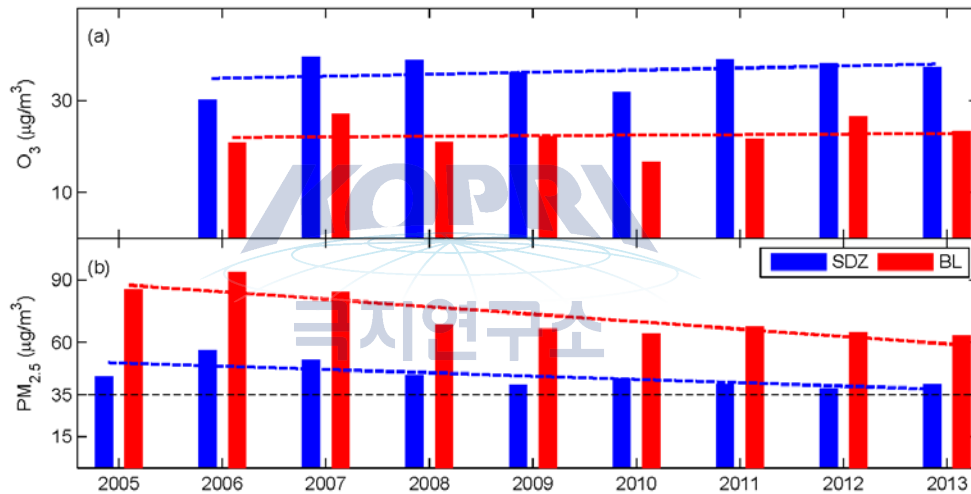


Fig. 2. Annual mean concentrations of O₃ (a) and PM_{2.5} (b) at SDZ and BL stations

(Long-term trends are shown as dotted lines; the black dashed lines in (b) indicated the PM_{2.5} at the minimum safe level for the residential areas)

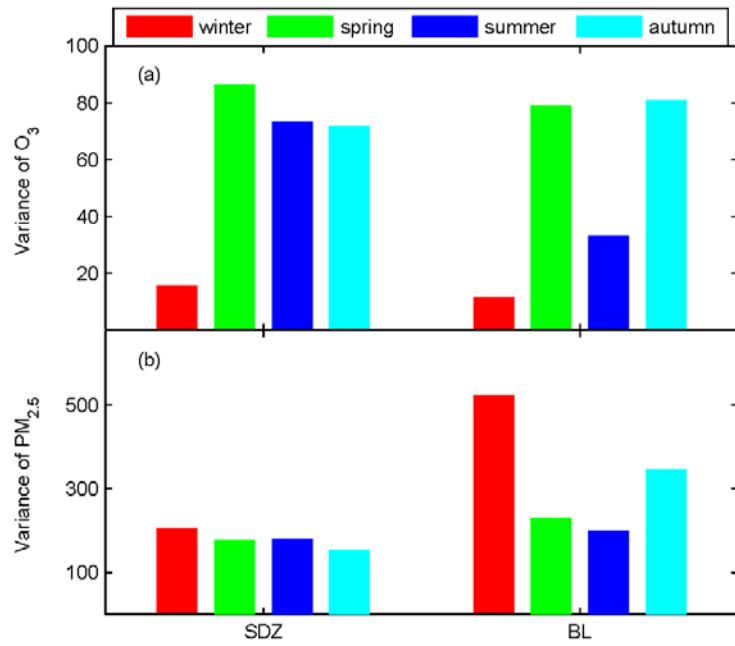


Fig. 3. Variances of the average daily variability of O₃ (a) and PM_{2.5} (b) in the different seasons for the two stations

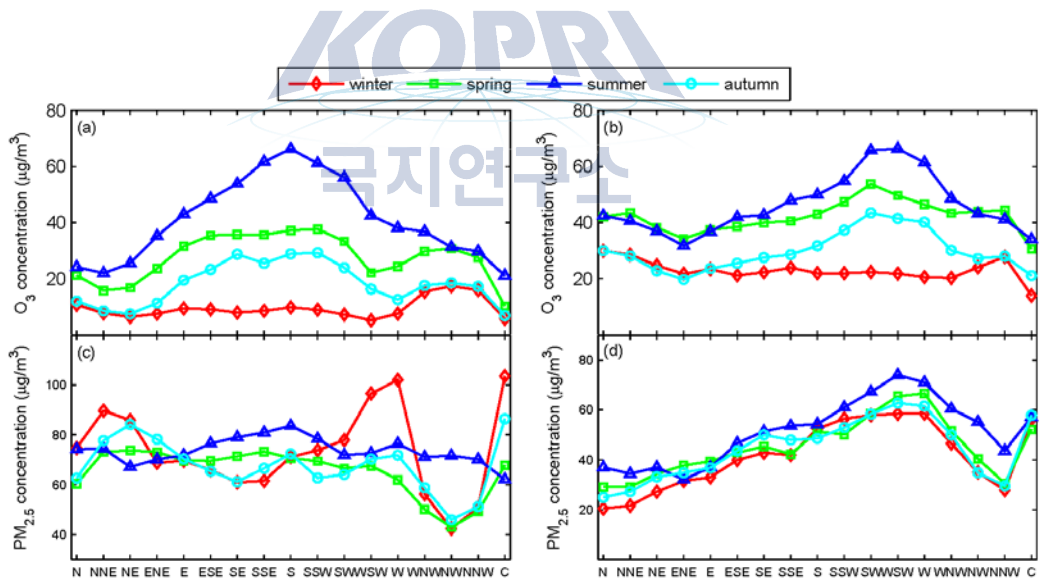


Fig. 4. Distribution of seasonal average concentrations of O₃ (a, b) and PM_{2.5} (c, d) at BL (left) and SDZ (right) stations in 16 directions (C denotes the concentrations on calm days)

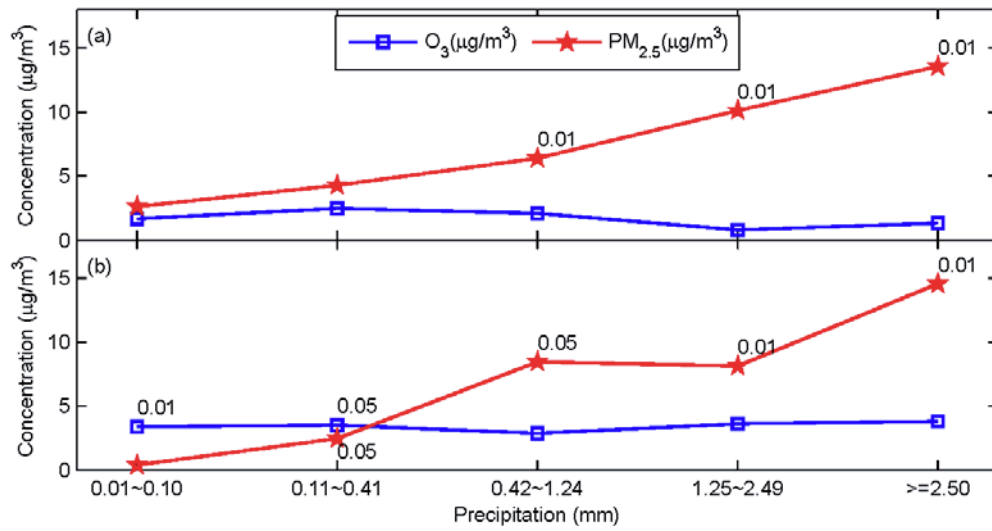


Fig. 5. Average hourly concentration differences of O₃ and PM_{2.5} between pre- and post-precipitation for each category of precipitation at the SDZ (a) and BL (b) stations (values shown in the figure denote the significance level of the differences)

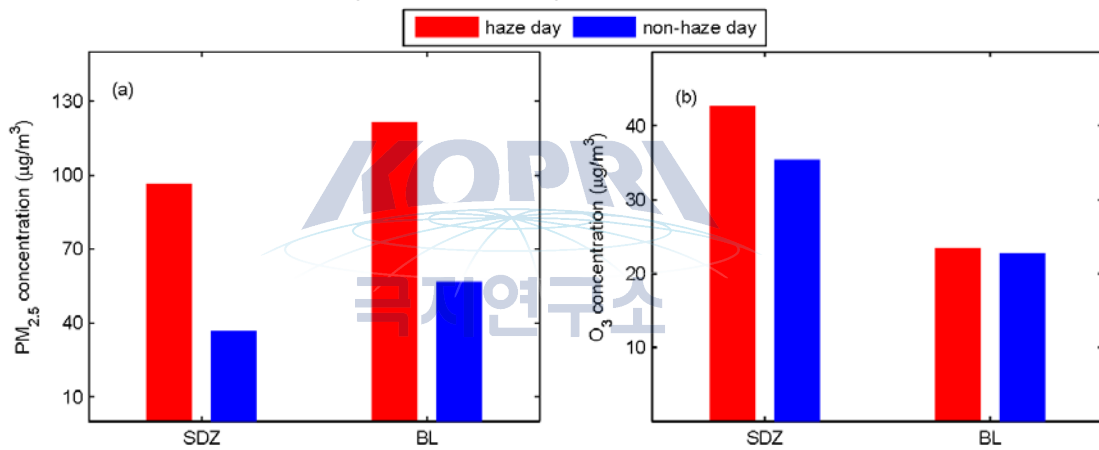


Fig. 6. Average daily concentrations of PM_{2.5} (a) and O₃ (b) on haze day and non-haze day (all of the differences were significant at the 0.01 confidence level)

8. *Related study funded by the KOPRI project: Does the recent warming hiatus exist over northern Asia for winter wind chill temperature?*

Motivation and goals

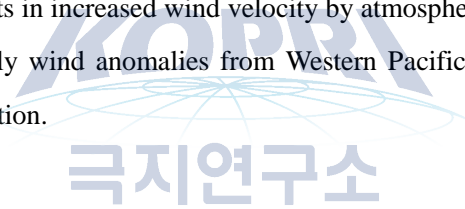
Wind chill temperature (WCT) index or wind chill index is a measure used to evaluate the joint effect of high wind velocity and low temperature on the exposed body skin; a low (high) WCT means a cold and windy (warm and less windy) weather. Asia is the most populated continent in the world where many people have experienced cold and windy weather in winter season, in particular for northeast Asia and Siberia (e.g., Analitis et al., 2008, Baccini et al., 2008, Rehill et al., 2015). Therefore, it is important to examine the changes in WCT over Asia, which provide information about potential hazard for human life and then could support policy makers to design policies for adapting the changing climate.

Many studies analyzed the long term trend in WCT and suggested that global warming may be the reason for the increasing trend in WCT from regional scale to continental scale. Recently, the Intergovernmental Panel on Climate Change Fifth Assessment Report pointed out that global warming has slowed down during winter season for recent 15 years (1998–2012) (Easterling and Wehner, 2009, Fyfe et al., 2013, Kosaka and Xie, 2013, Trenberth et al., 2014, Fyfe et al., 2016). In addition, variations in wind velocity also show different patterns before and after 1998 over China, i.e., a long-term decreasing trend before 1998 and a nearly zero trend afterward (Lin et al., 2013). The combined effect of the increasing (decreasing) trend in air temperature together with the decreasing (nearly zero) trend in wind velocity before (after) 1998 over China indicates an increasing (decreasing) WCT trend over China before (after) 1998 may occur. This result indicates that there exists a warming slowdown (i.e. hiatus) of WCT in recent decade after 1998 compared to the period before 1998 when there was the warming trend of WCT. In this study, we analyze the changes in WCT index over northern Asia since 1973 to examine whether there is a warming hiatus of winter WCT during 1998 to 2013.

Work done and findings

Based on the observational data from 1973-2013, we investigated the changes in the trends of winter WCT over the Tibetan Plateau (TP), the Far East (FE), and the rest of northern Asia (RA). The results show that as compared to the increasing trend in WCT during 1973-1998 (P1) over northern Asia, the winter WCT experiences warming hiatus in the TP and RA from 1999 to 2013 (P2) and the cooling tendency over RA during P2 is significant. For Far East, the winter WCT continues heating up. The causes

of the winter WCT variation over the TP, FE and RA are different. Over RA, the temperature plays a dominant role in winter WCT trend (Table.1). Further analysis indicates that the hiatus of winter WCT over RA is a result of the atmospheric circulation anomalies in the low and mid troposphere. As compared to the circulation in P1 epoch, there are positive height anomalies over Siberia and negative height anomalies over the area in the north of Tibetan Plateau (western Mongolia) during P2 at sea level pressure (500 hPa). This distribution of height anomalies results in an increased pressure gradient from high latitude to mid latitude during P2, which is favorable to make the cold air transport from high latitude to middle latitude and therefore low air temperature over these regions. Over the TP, both temperature and wind speed are important to winter WCT trend. The temperature keeps rising during P1 and P2 period, however, the wind speed presents a decreasing (increasing) trend during P1 (P2) period. The increasing in wind velocity offsets the increasing of air temperature during P2 period, resulting in a nearly zero trend in WCT and therefore a slowdown as compared to the increasing WCT during P1 period. The increase of temperature over the TP may be caused by more solar radiation due to the depletion of ozone and decrease (increase) in daytime (nighttime) cloud amount. The increase of wind velocity during P2 may be caused by the increasing of height gradient and air temperature between the regions to the south and to the north of the TP at 500 hPa level, which results in increased wind velocity by atmospheric thermal adaption. For the Far East, southerly wind and easterly wind anomalies from Western Pacific makes the temperature heat up during P2 period by warm advection.



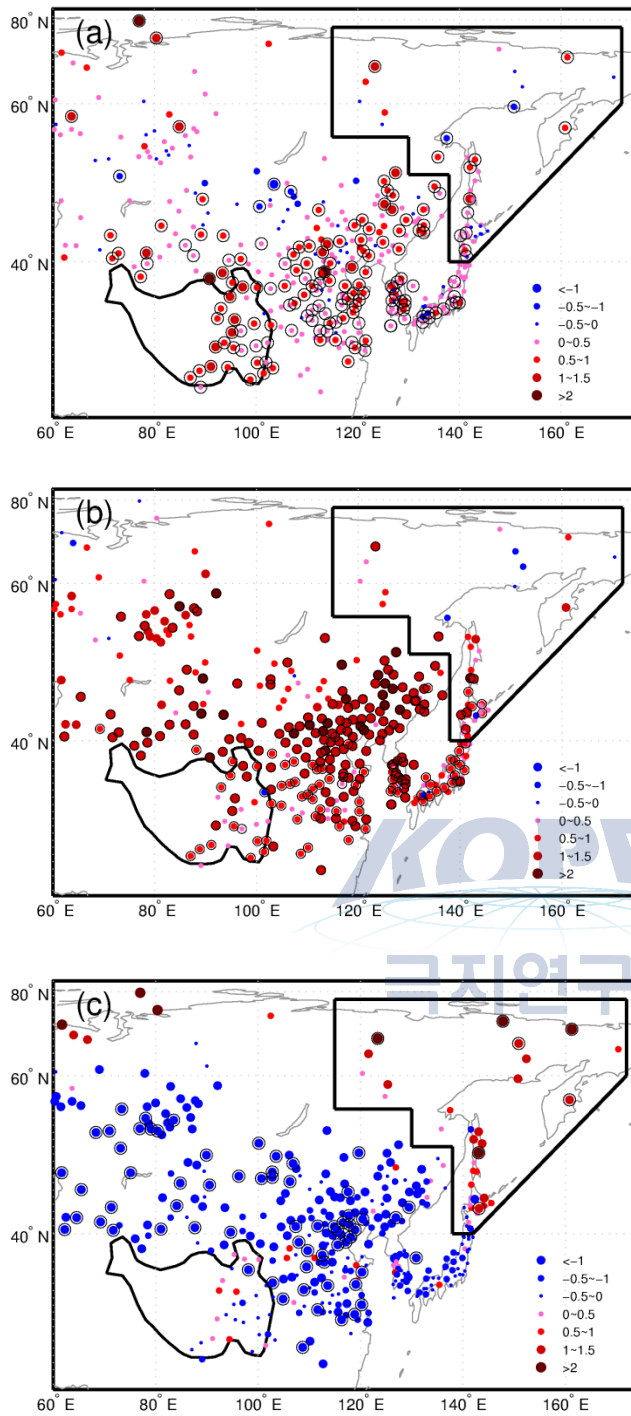


Fig.1 Spatial distribution of winter WCT trends over Northern Asia. (a) Period 1973-2013. (b) Period 1973-1998. (c) Period 1999-2013. The circled points indicate that trends are significant at the 95% confidence level. units: °C/decade. Stations enclosed by solid contour line on the left of the map belong to the Tibetan Plateau. Stations enclosed by solid contour line on the right of the map belong to the Far East.

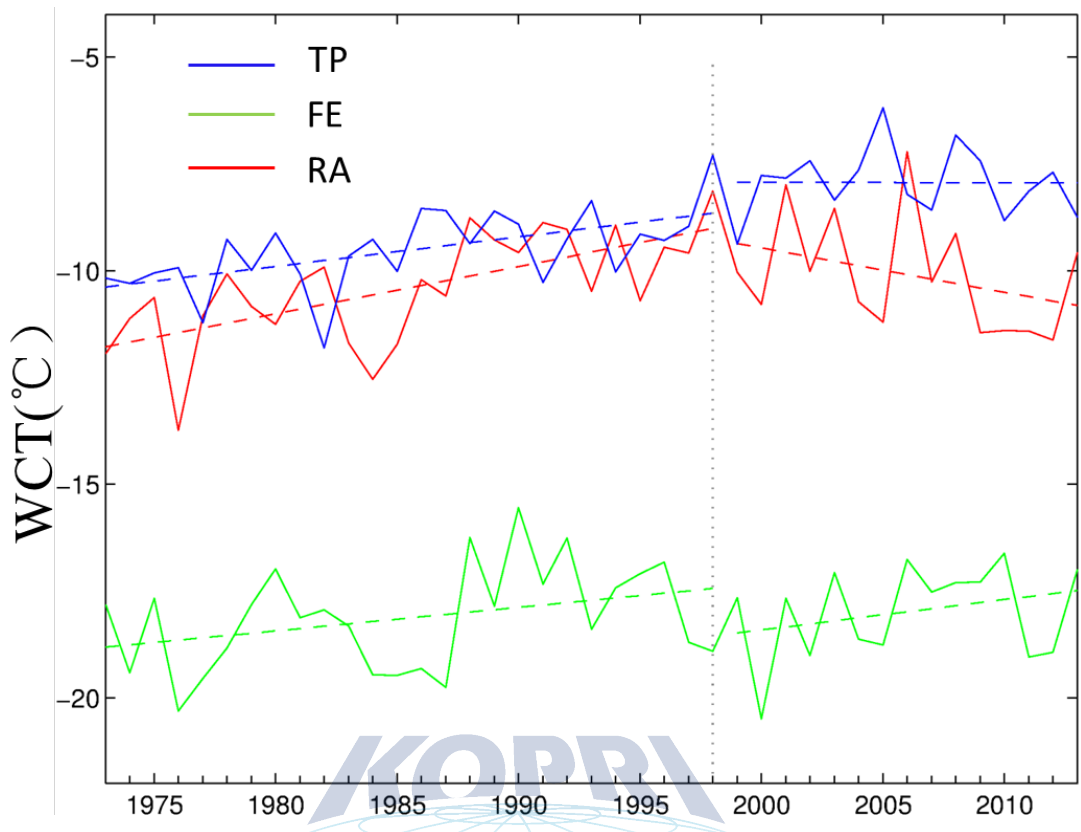


Fig.2 Anomaly time series of average winter WCT over the Tibetan Plateau (TP), Far East (FE) and the rest of Northern Asia (RA). The blue (green) curve represents winter WCT over Tibetan Plateau (Far East) and red curve indicates the winter WCT over the rest of Asia. Dashed lines indicate the linear trends.

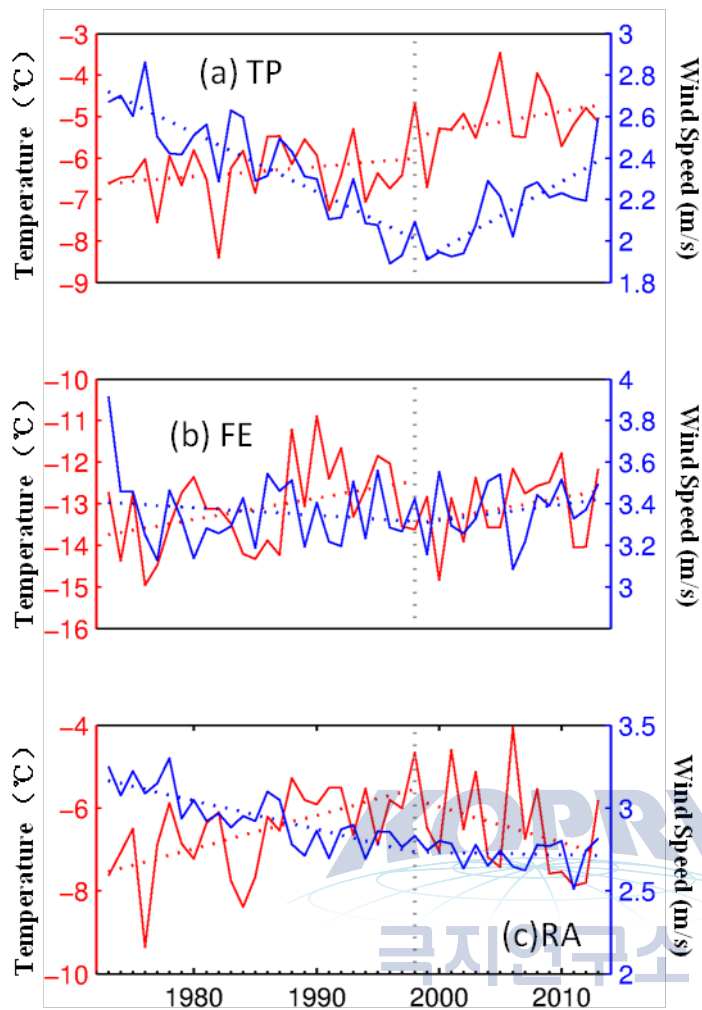


Fig.3 Time series of average air temperature and wind speed in winter (DJF) over TP (a), FE (b) and RA(c).

The red curve represents air temperature trend, and blue curve indicates the wind speed trend over the Tibetan Plateau (TP), Far East (FE) and rest of Northern Asia (RA), respectively.

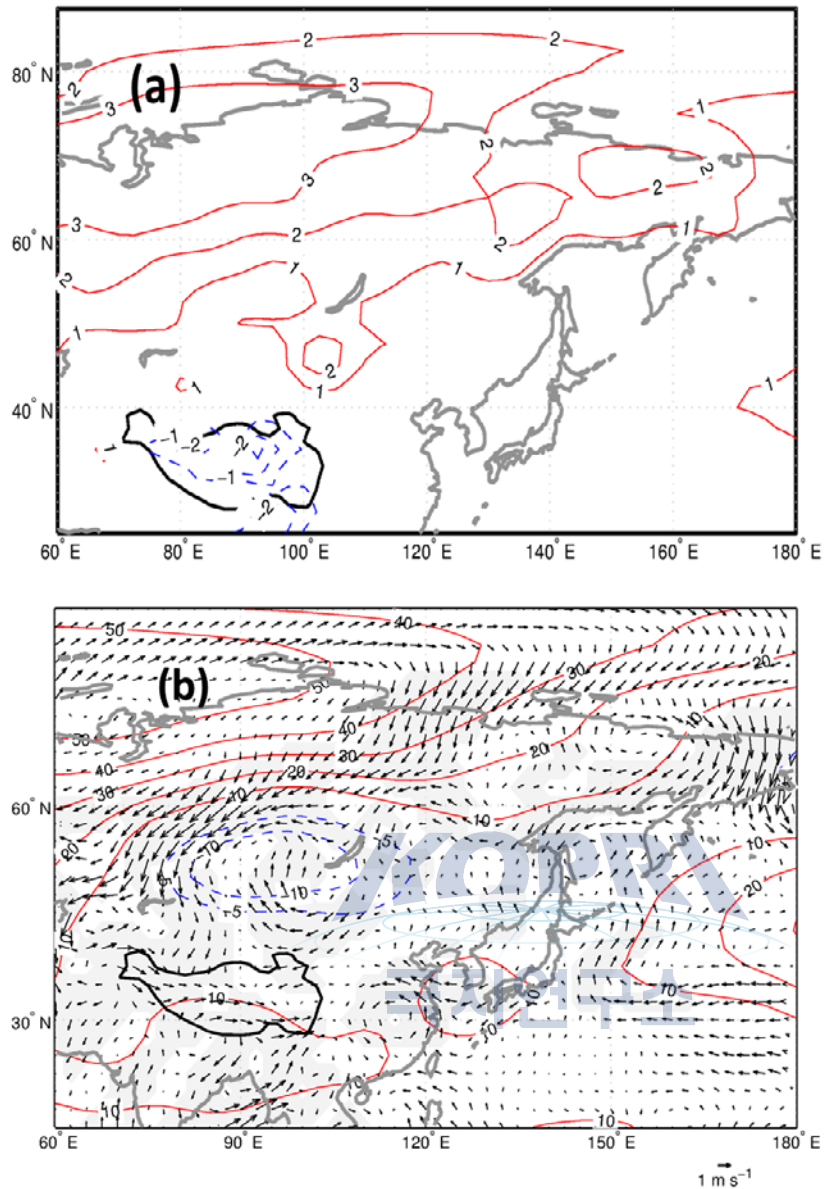


Fig.4 Sea level pressure (a)(hPa; blue dashed are negative, red curves indicates positive) (1999-2013 minus 1973-1998). And composite of winter (DJF) (b) 500-hPa geopotential height (hPa) and 925-hPa wind field (m s⁻¹; the shaded is statistically significant at the 95% confidence level.) (1999-2013 minus 1973-1998).

Black curve indicates the Tibetan Plateau.

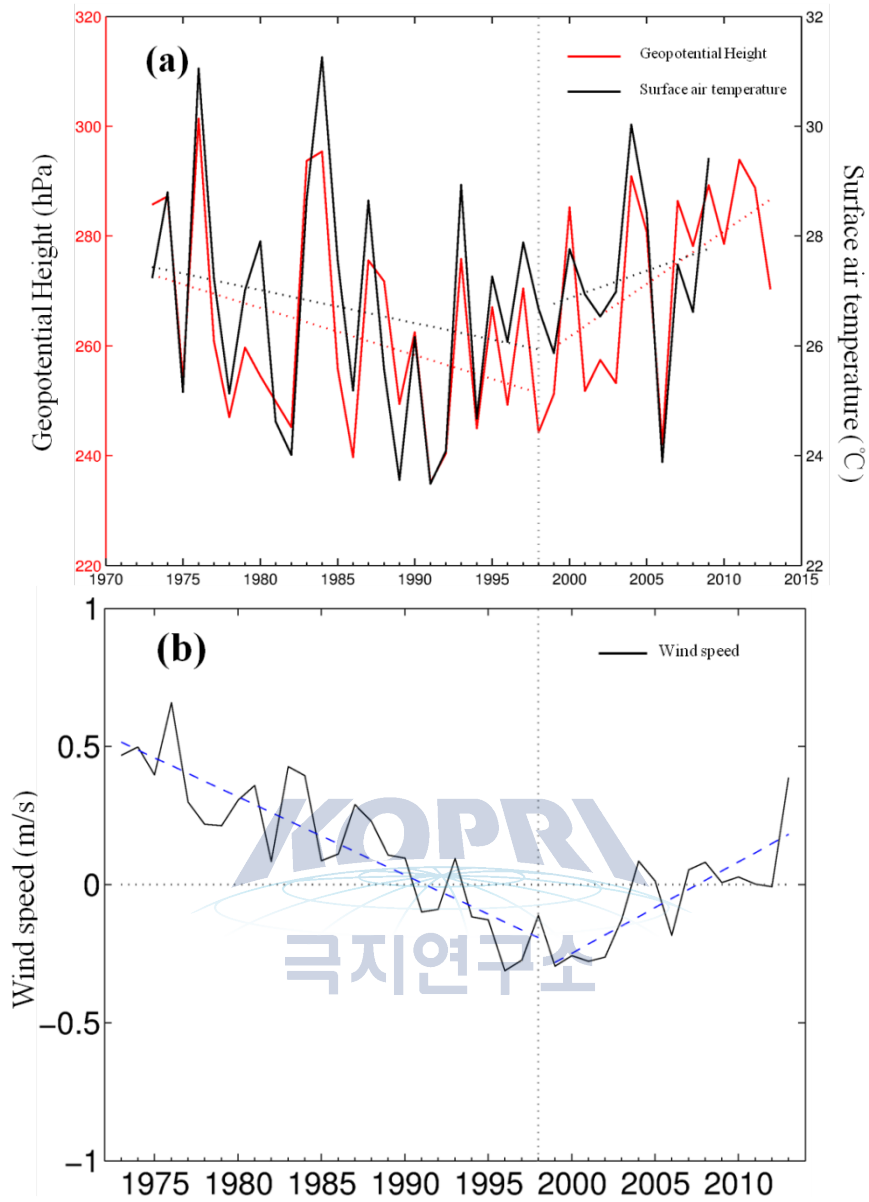


Fig. 5 Difference of winter geopotential height at 500-hPa level (1973-2013) and surface air temperature (1973-2009) (a) between region 1 (20° - 25° N, 80° - 102.5° E) and region 2 (45° - 50° N, 80° - 102.5° E) (red curve represents geopotential height and black curve indicates surface air temperature; dashed lines indicate the trend) and wind speed trend (b) (blue dashed lines indicate the trend for pre-1998 and post-1999).

주 의

1. 이 보고서는 극지연구소 위탁과제 연구결과보고서입니다.
2. 이 보고서 내용을 발표할 때에는 반드시 극지연구소에서 위탁연구과제로 수행한 연구결과임을 밝혀야 합니다.
3. 국가과학기술 기밀유지에 필요한 내용은 대외적으로 발표 또는 공개하여서는 안됩니다.